University of South-Eastern Norway
Faculty of Technology, Natural Sciences and Maritime Sciences

Master's Thesis

Study programme: Master of Science in Micro and Nano Systems Technology

Spring 2023

Sander Hasle

Improved quality factor on lamb wave resonators using a phononic crystal structure array

For High Frequency Lamb Wave Resonators

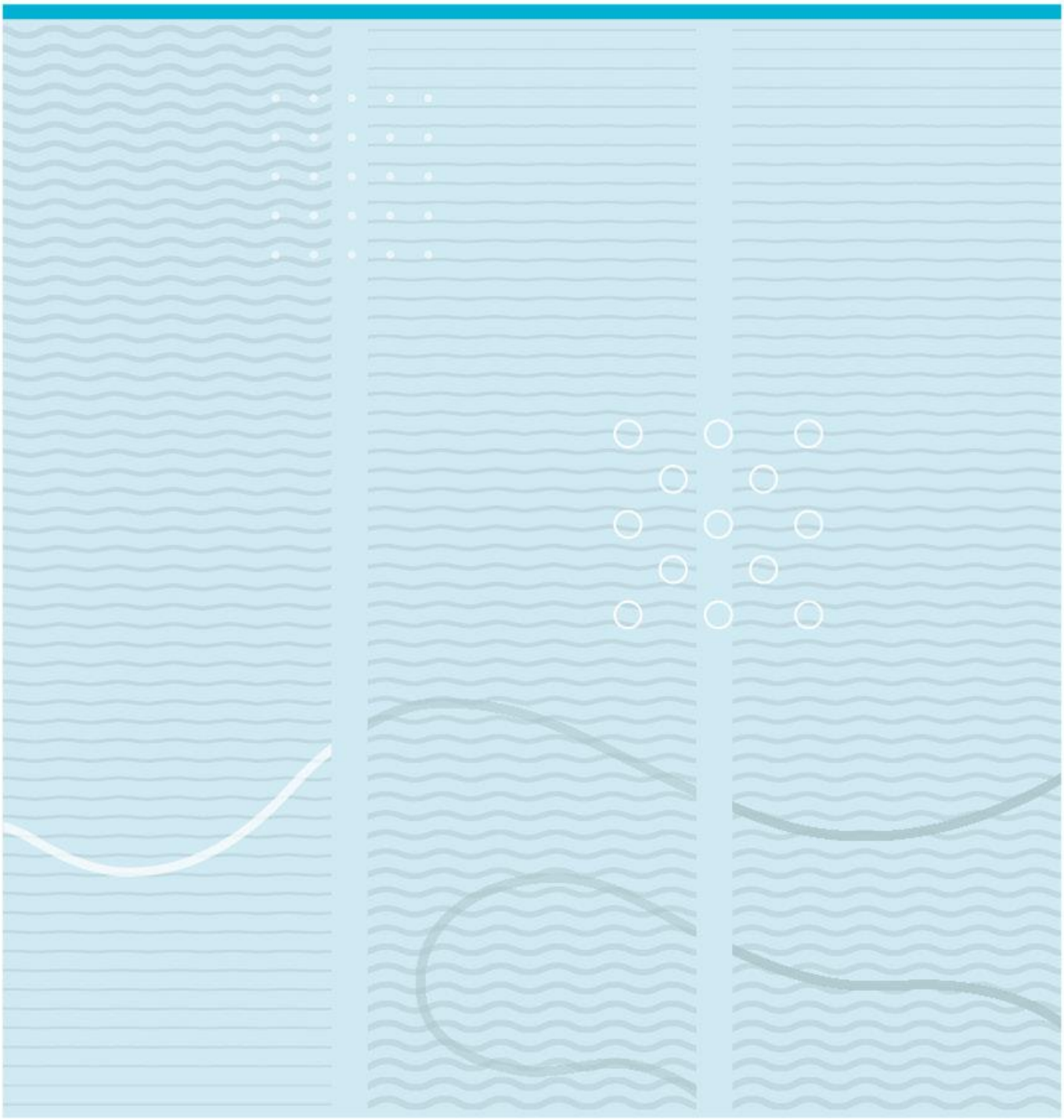

University of South-Eastern Norway
Faculty of Technology, Natural Sciences and Maritime Sciences
Department of Microsystems.
Raveien 215
NO-3184 Borre, Norway

http://www.usn.no

University of South-Eastern Norway

www.usn.no

Course: *MN-FIN5000-1 Final Project 2023*

Title: *Improved quality factor on lamb wave resonators using a phononic crystal structure array*

Keywords: *AlN, $LiNbO_3$, LWR, Quality Factor, PCS, S0, SH0*

Pages: *81*

Student: *Sander Hasle*

Supervisors: *Ulrik Hanke, Hamed Salmani*

Summary:

This thesis explores the possibility of increasing the quality factor of a lamb wave resonator device with the use of a phononic crystal structure array on the surface of the bridge suspending the device.

In the growing industry of telecommunication, there is an increasing demand for high performance devices. As the amount of data transmission is rapidly increasing year on year, so is the need to implement higher frequency bands. Therefore, the demand for smaller devices which can operate in the GHz frequency range, has accelerated the research of lamb wave resonators.

This because they have the possibility of a highly adaptable frequency response based mainly on the geometrical structure of the device.

The Ain structure is a widely used material for both surface acoustic wave and lamb wave resonator devices. It offers a high phase velocity, mechanical strength, chemical inertness, and thermal stability making it very suitable for high frequency devices. However, in recent years there has been a push to explore the possibility of using lithium niobate and lithium tantalate for its higher mechanical coupling factors. Making the possible use of high-end devices quite attractive, regardless of the higher production cost.

Here we investigated the design prosses of a FEM simulation using COMSOL Multiphysics for the purpose of optimising and predicting the response rate of a lamb wave resonator using different materials. Both designing relevant boundary conditions as well as relevant simulations are investigated.

Acknowledgements

I'm very grateful for everyone who have been a part of my learning journey during my degree. I have had so many interesting and engaging interactions, all a big part of the great learning environment at USN. The support from every fellow student and professor have played a crucial role in making it possible for me to get this far.

I would also like to offer my sincere gratitude to both my main supervisor Ulrik Hanke and co-supervisor Hamed Salmani. Their contribution to the process and the thesis has been instrumental. Along the way they have helped me with different challenges; from small quick discussions to taking the time helping me with bigger challenges over the course of the last year.
I am extremely grateful for both the time they gave me and the effort they took to help me.

Lastly, I would like to thank all my family for being an endless source of encouragement and support. I wouldn't be where I am today if it wasn't for them.

My utmost and sincere gratitude to everybody who have been a part of making this possible.
I thank you.

Vestfold, 22nd May 2023
Sander Hasle

Contents

List of figures

List of Tables

Nomenclature

SYMBOL	EXPLANATION
AIN	Aluminium Nitride
BAW	bulk acoustic wave
BEM	Boundary Element Method
K_{eff}^2	Effective electromechanical coupling coefficient
ECM	electrical equivalent circuit model
FEM	finite element method
HFR	High Frequency Range
IDT	Interdigital Transducer
$LINBO_3$	lithium niobate
LWR	Lamb Wave Resonator
MCS	Mesh Convergence Study
PCS	Phononic Crystal Structure
SAW	Surface Acoustic Wave

1 Introduction

1.1 Lamb Wave Resonator Motivation

The science of telecommunication is an ever-evolving field of science. One could say it started as early as 1816 with the first working telegraph built by Francis Ronald's [1]. And the bar continues to be raised regarding what to expect from a working telephone, from simply having messages delivered, to uploading and downloading large data files [2]. This change naturally drives the demand for a faster broadband cellular network and is the main reason we have gone from 1G first-generation cellular network to the modern 5G fifth-generation cellular network in a relatively short timeframe. There is no doubt this is still a growing field and the need for better resonators is a largely studied field, with now the objective to try and push this technology to its sixth generation [3].

In this project, we will investigate the possibility of improving the parameters of a LAMB wave resonator (LWR), with the inclusion of patterned phononic crystal structure (PCS) design on the anchor sections of a LAMB wave resonator (LWR). One main driver for looking into this is the large energy loss this system experiences over the bridge section of a device. This is one of the big limiting factors on a LWR as the largest energy loss can be found over the bridge. Making the device response a heavily hampered version of its possible response. As the acoustic waves generated in the resonator travel through the bridge and leak through the anchor of the device.

Where this would also allow us to use substrate made of Lithium Niobate ($LiNbO_3$) instead of the more commonly used Aluminium Nitride (AIN), where $LiNbO_3$ commonly offers a much larger effective electromechanical coupling coefficient (K_{eff}^2) then its counterpart AIN [4], [5].

To limit this we are looking into the possibility of using phononic crystals to stop the transmission of energy through waves in a medium, mainly over the bridge section of a device [6]. This would make it possible to create a barrier on the bridge section with a PCS array, thus making it theoretically possible stop the energy leakages completely throughout the bridge. In doing this we would improve the parameters on any given LAMB wave resonators without giving large restrictions in the used materials or structure parameters. The main challenge in this project therefore lies in designing these phononic crystal structure on top of the bridge and to investigate the effect they can have on the functionality of the LWR. This will be done by simulation, as it allows us to test the theoretical possibility of these implementations on a broader scale compared to an individual scale of a physical fabrication test. By doing this we can look past errors coming from physical

imperfections under the creation of a device. However, we will still be designing our devices with its potential future creation in mind.

1.2 Model

There has been an array of different modelling techniques in continuous development in the history of mems design. This is due to the importance of testing the design of the new structure in a reliable and efficient way, before initiating the long and expensive production of the device.

Where it started with relatively simple models, like the impulse response model also called delta function model (δ-model) and the electrical equivalent circuit model (ECM). Delta model utilizes the concept of superposition, where it can define each electrode of the IDT as a separate periodic delta function. However, it is not able to include part for the reflections, making it unsuited for low-loss filters as this is a key component of their functionality. ECM is a more robust modelling method. It has over time been extensively improved to include concepts like reflection from mechanical and electrical load, electrode edges and energy storage.

The requirements on performance and complexity of acoustic wave device like SAW devices and LWR devices have increased drastically over the years. This has accelerated the need to create and use more advanced modelling techniques. One method being the coupling-of-modes (COM) theory, that is defined as a set of differential equations. Another established method is the P-matrix model (PMM) introduced by Tobolka [7]. The main problem with the above-mentioned models is that they are physiological simulations that require accurate parameters to deliver good results.

Another feasible method is to use numerical tools that calculate the device properties directly from the material and geometry parameters. This would make it possible to easily calculate the device response more accurately for a wide range of different materials and geometrical parameters. The most common forms of these techniques are the finite element method (FEM) and the boundary element method (BEM). The problem has been that these methods are very time consuming when doing simulations on more complex cases such as a LWR device. Even with today's computing the simulation of a complex system can be very time consuming as it often requires millions of separate calculations to be done for a simple data point.

But even after considering the limitations with FEM simulations, it remains the most reliable method to produce a result considering the task at hand. Based in this, we will be looking into the possibility of using COMSOL Multiphysics to simulate an accurate response rate for a LWR device

and explore the possibility of improving the response rate with the use of a phononic crystal structure array.

1.3 Material

One of the most important part of any resonator device design is in the material selection [8]. Where a selection must be made considering the device application and potential device respond. Here a selection must be made so that the device can be stable in its use environment [9]. However, in a resonator device there is also a high importance of choosing a material with a suitable coupling coefficient, temperature coefficient, phase velocity, phase velocity dispersion and K_{eff}^2. So, for this reason the use of AIN as it holds a wide range of desirable properties for the use in a resonator device. Where it holds a high phase velocity of up to 10000 m/s, a weak phase velocity dispersion, a small temperature coefficient and an small to moderate K_{eff}^2 [10]. As the response of a SAW resonator device is mainly limited by the material parameters. Materials like AIN have been heavily used for these devices, the main problem here is that AIN offers only a small to moderate K_{eff}^2. However, with AIN having a relatively ease of production with a low production cost, it has been the most commonly used material for general application [11]. But with the rise in demand for ultra-high frequency based resonators, more studies have been looking into the potential of more suited materials for these devices [12]. One of these materials being $LiNbO_3$, this comes from the fact that it shares a lot of useful qualities with AIN. As it also holds a high phase velocity, low phase velocity dispersion and a low temperature coefficient. But where AIN holds a moderate K_{eff}^2 of 7%, $LiNbO_3$ YX36°-cut cut hold a much larger K_{eff}^2 of 31.7% [4]. While in Silvan Stettler's paper, they found their $LiNbO_3$ YX36°-cut cut LWR device to have an K_{eff}^2 as high as 29.7% [5]. However, as AIN is far easier and cheaper to fabricate it has remained far more used and researched to this date.

Because of this similarity these two materials have been chosen for further studies in the FEM simulation designed. Where aluminium was chosen to use for the metallic layer and platinum for the PCS slab. As Platinum has a large density relative to the other materials makes it highly suited for the use in creating a large PCS bandgap. While aluminium offers a very similar density compared to the piezoelectrical material, hopefully reducing its impact on the PCS bandgap. All the used material parameters for the FEM simulations can be found in appendix c below.

1.4 Motivation

As mentioned above, the demand for better and faster data transfer is rapidly increasing. This has been the main driving force behind the push for improving components used in telecommunication [13]. For large parts of late 19th and early 20th century, the telecommunication industry researched heavily into the optimization of SAW devices. As they offered a relatively easy fabrication process with a wide array of cheap and varied material selection [14]. However, with the increasing demand for a better telecommunication device the demand for high end resonator devices becomes more prevalent. This is where the potential of a LWR device started to get some attention. As its high dependency of geometrical properties to define the frequency response of the device would allow a design more suited for wide bandgap high frequency range (HFR) filters [15]. This would allow for the use of materials like $LiNbO_3$, for its very high K_{eff}^2 compared to a more traditional material used in SAW devices, like AIN [16].

Some of the earlier studies into optimizing the quality factor of an LWR device by reducing the energy leakage of the device was done in 2015 [10]. In recent years there have been a large increase in the number of studies done on the potential of using LWR devices for HFR. Where the common idea is to explore the possibility of getting an increase in quality factor on the resonator device through stopping the energy leakage happening over the bridge section of a device [17]. Different methods have been tried out, from the adding of a butterfly shaped geometry on the side of the bridge section, to creating a saw pattern for the bridge section. However, most suffer from the fact that they will have a negative impact on the design options of the device. As they require a very precise manufacturing processes to potentially see an increase in the quality factor of the device. And would require small and hence fragile bridge structures. This would make these optimizations only viable for very small devices. This would then defeat the entire purpose of using a LWR device over a SAW or bulk acoustic wave (BAW) device. As it would limit the amount of Interdigital Transducer one could design a device with, and hence reduce the ECC of the device. To negate this the idea of using a phonic crystal structure (PCS) on the bridge structure has been explored. The benefit would be to stop the wave propagation over the bridge structure within a designed frequency region [18]. This idea offers a significant potential for an increase in the device quality factor with no design restriction on the bridge section of the device. As if done properly this would efficiently stop any wave propagation over the PCS array, making it possible to use long and sturdy bridge sections for the device. Giving the device a better physical integrity while maximising

the K_{eff}^2 of the device. So, this is a large inspiration for the purpose of this thesis to investigate the possibility of creating an increased quality factor in a LWR device using a PCS array.

1.5 Outline of the Thesis

Section 1 outlined an introduction to LAMB wave resonator history and the beginning of the device technology. It discusses how LMR has slowly began appearing in the consumer market. And it goes into the chosen material and modelling techniques chosen for this study. And some outlining motivation for this study.

Section 2 introduces the fundamental principles for a LWR device, together with very basic theory surrounding elastic wave propagation in solids, piezoelectricity, tensor transformations, Bloch wave theory and mesh convergence theory.

Section 3 goes into the development of the COMSOL simulations used in this study. Where we will go into the chosen boundary conditions set in these FEM models and physical parameters set for the simulations. We will also go over the geometrical parameters used for the different FEM models, and the studies done on each FEM model.

Section 4 Presents the gathered test data and the different parameters found using these COMSOL simulations. Here the main results of this study can be found and talked about.

Section 5 covers the discussion part of the thesis, where we will go over outliers from the previous section that could not be reasonably covered earlier. We will also briefly touch upon some future potential for PCS array.

Section 6 is a short conclusion of this thesis, giving a short summarization of the main takeaway from this thesis.

2 Fundamental Principles and Theory

2.1 Fundamental Lamb Wave Resonator concept

The fundamental idea of any Lamb wave device, including a resonator, is to induce Lamb waves withing a structure, in the transverse and longitudinal directions. One of the most common ways to achieve this is with the use of electrodes places on a piezoelectric material, as this is a simple yet effective way to couple electrical and mechanical energies together. These metal electrodes are referred to as the interdigital transducer (IDT) and is one of the two major variables resulting in the flexibility of design Lamb wave resonators (LWR) have. The other major characteristic one can change of a Lamb wave resonator to change its response is its substrate geometry, mainly the IDT geometry, this is also one of the major upsides of using a LWR over a more traditional SAW waves resonator (SWR). Both resonators will have the benefit of being affected by the substrate material, IDT geometry and IDT numbers. But a LWR will have the added benefit of being able to heavily change its frequency response with changing only its device geometry, something which gives it a far wider flexibility compared to a SWR design.

In this project we are using a variation between positive and negative electrodes on the surface of a piezoelectric device to create the Lamb waves, this can be seen in the figure below. This will create longitudinal Lamb waves in the transverse direction of the electrodes, and as the Lamb waves will diffract it will also create transverse Lamb waves along the electrode and device.

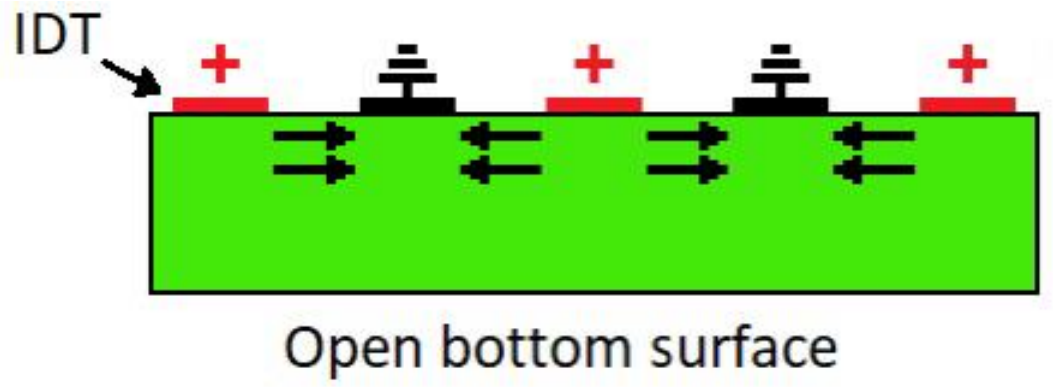

Figure 2.1 Illustration of the IDT layout

And as Lamb waves travel inside the material it is possible to induce a large change in a device frequency response simply by changing its electronic pitch (EP). This is a large advantage Lamb wave resonators have above a SAW device, as a SAW device will have a far less flexible frequencies

response change based on the geometrical design of the device. However, as Lamb waves travel inside the material this induces a large loss on the device over the bridge holding the device. And in a resonator device keeping leakage energy as close to zero is ideal to get a clear and precise device response. This comes from the fact that a reduces leakage would introduce a larger displacement under a desired mode, and just like how a large electric signal over the IDT would incline a large device displacement so would a large produce a larger electric response. So, with a reduce leakage over the bridge we could get a larger and more accurate response form the device. Hence, the premise of this thesis to reduce acoustic wave leakages over the bridge structure with the use of a phononic crystal structure design.

2.2 Elastic waves in solid

Theory around elastic waves in solid is a crucial topic to cover, as it is the groundwork on which Lamb wave theory is built upon. So, to start this we would investigate the topic were the criteria that the wavelength of the elastic waves is much larger compared to the interatomic distance, this would let us consider any homogeneous solid as continuous. And if we assume that the solid is elastic, it will mean that any internal forces would cause no permanent deformation with respect to the equilibrium state of the solid. And continuing with this and making the statement that any pure translation and rotation of the material will not cause rise to any internal forces, we can use the general definition of strain (S_{kl}) which excludes these types of displacements as [19].

$$S_{kl} = \frac{1}{2}\left(\frac{\partial u_k}{\partial x_1} + \frac{\partial u_l}{\partial x_k}\right) \qquad k, l = 1,2,3 \tag{2.1}$$

Where strain is a 2nd rank tensor, where u represent the displacement functions in the x_1, x_2 and x_3 directions. And the sum of the partial derivation in equation (2.1), showing the strain tensor must be symmetric with.

$$S_{kl} = S_{lk} \tag{2.2}$$

The internal forces present on the material can be represented by a general stress tensor (T_{ij}), where as the stress is defined by the force per unit area. The stress tensor is also of a 2nd rank and can be shown to be symmetric.

$$T_{ij} = T_{ji} \qquad (2.3)$$

Then by using the well-known Hook's law with the previously definition it is possible to relate the internal forces and deformations as a generalization of this law [19].

$$T_{ij} = c_{ijkl} S_{kl} \quad i,j,k,l = 1,2,3 \qquad (2.4)$$

Here c_{ijkl} is a rank 4 tensor referred to as the stiffness tensor. As in traditional uniaxial Hook's law the material constant defines the relation between the stress and strain in a similar fashion as Youngs' modulus (E) would. In both equation (2.4) and the following equations Einstein notation of summation over repeated indices is applied. Where even if the stiffness tensor generally includes 81 components, because both the stress and strain tensors are symmetric, so too is the stiffness tensor symmetric.

$$c_{ijkl} = c_{jikl} \quad and \quad c_{ijkl} = c_{ijlk} \qquad (2.5)$$

It is possible to drastically reduce the independent elements for different materials by taking certain thermodynamic considerations and specific crystal symmetry into account. And example of this would be a material with a cubic symmetry, as here it would only have three independent constants of the total 81 components. And with the fundamental term in place, we would only need to include the time variation next.

As the wave travels throughout the medium, it would have to have a local displacement that changes with time, and as all these motions need to obey Newton's laws. Therefore, the net forces would be equal to the mass multiplied acceleration. And the relation is typically referred to as the equation of motion and is given as.

$$\rho \frac{\partial^2 u_i}{\partial t^2} = \frac{\partial T_{ij}}{\partial x_j} \quad (2.6)$$

Here the ρ is the mass density and the volume terms have cancelled out. Then by substituting equation 2.1 and 2.4 into 2.6, and applying the condition in 2.5, the general wave equation for elastic waves in a non-piezoelectric solid can be given in the typical form [19].

$$\rho \frac{\partial^2 u_i}{\partial t^2} = c_{ijkl} \frac{\partial^2 u_l}{\partial x_j \partial x_k} \quad (2.7)$$

2.3 Piezoelectric Materials

When considering the physics for a piezoelectric material, one need to consider more than just the coupling between the mechanical stresses and strains. As the displacement changes becomes more complicated as we now need to consider the effect these changes have on the effect on both the displacement forces and electrical fields applied. To start this of we would start with the definition of electric displacement field for free charges as done in reference to Vegard Tollefsen work [20].

$$D = \varepsilon_0 E + P \quad (2.8)$$

Here ε_0, E and P is the vacuum permittivity, the electric field, and the polarization density respectively. Then by considering only a simplified one-dimensional model, with a constant electric field and applying Gauss's law it is possible to show that the changes in polarization density can be written as the change in bound charge density. So, by using the simplification of a one-dimensional system like done in the figure below, we can write.

$$\Delta P = \frac{nq(\Delta a - 2\Delta b)}{2} \qquad (2.9)$$

In this simplification n is the number of opposite charge pairs per unit volume, q is charge, Δa the cell deformation and Δb is the change in distance between the opposite charges. We can visually see this illustrated in the Figure below with the first case being at rest and the second case an electric field is applied. From this is can clearly understood that this material is piezoelectric and must have a net dipole different from zero, where q^+ can be assumed to be equal to q^- since $b \neq \frac{a}{2}$. So, from the electrostatic force equilibrium for one charge, we can write the expression for Δb as.

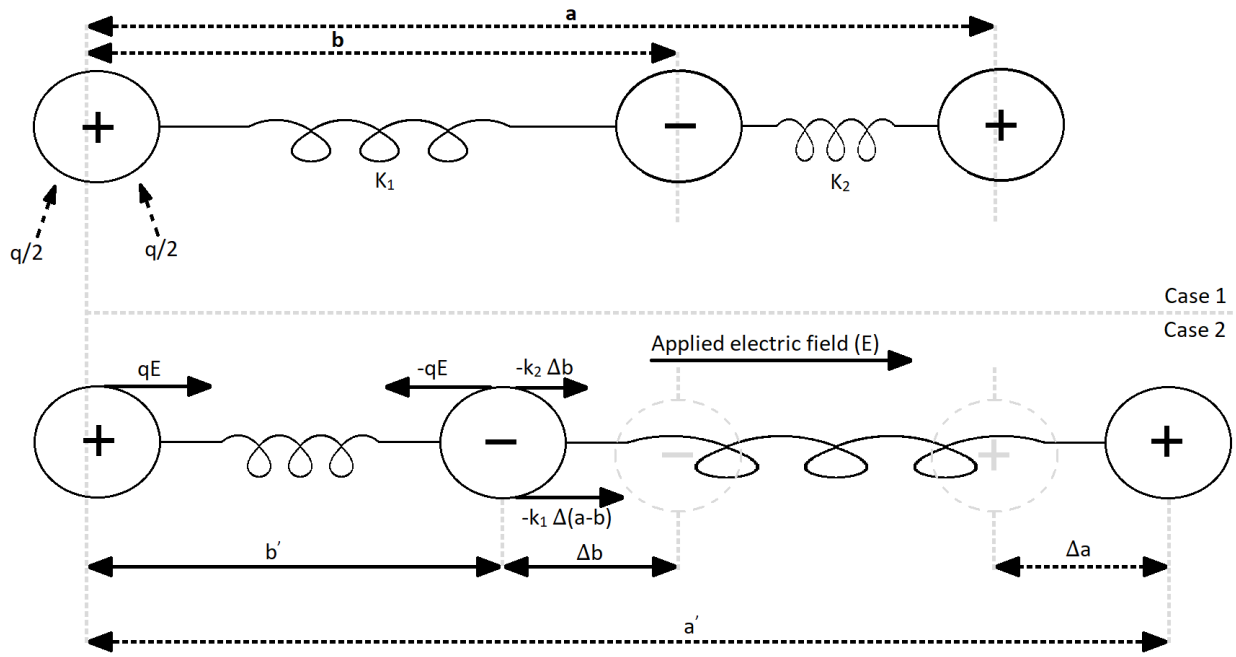

Figure 2.2 Piezoelectric effect

$$\Delta b = -\frac{qE}{k_1 + k_2} + \frac{k_1}{k_1 + k_2}\Delta a \qquad (2.10)$$

We can change the form of the change in polarization density by substituting equation (2.10) into equation (2.9), doing so gives us it in this form.

$$\Delta P = \frac{nq^2}{k_1 + k_2} E + \frac{nqa(k_2 - k_1)}{2(k_1 + k_2)} \frac{\Delta a}{a} = \chi_{ion} E + eS \qquad (2.11)$$

Here we can see that one term is proportional to the electric field and the other term proportional to the strain in the form $\frac{\Delta a}{a}$. Were χ_{ion} is the ionic susceptibility and e the piezoelectric constant. k_1 and k_2 represents the different spring constant associated with this asymmetric system. And by again substituting equation (2.11) into equation (2.8) and adding the electronic susceptibility χ_{ion} as it is not already considered in that model, we can obtain the following form of the electric displacement.

$$D = \varepsilon E + eS \qquad (2.12)$$

Were ε is the permittivity constant and is defined by.

$$\varepsilon = \varepsilon_0 + \chi_{ion} + \chi_e \qquad (2.13)$$

By generalizing equation (2.12) to three dimensions and define it in tensor form we get.

$$D_i = e_{ikl} S_{kl} + \varepsilon_{ij}^S E_k \qquad (2.14)$$

Here e_{ikl} is an 3rd rank piezoelectric tensor and ε_{ij}^S is an 2nd rank permittivity tensor. And by looking at the superscripts we can see that it indicates that the coefficients are given for constant strain. Here again the strain tensors are symmetric, so we can write the following piezoelectric tensor relations.

$$e_{ikl} = e_{ilk} \qquad (2.15)$$

A similar approach can be used to obtain the relation between the stress and the electric field by considering the traction instead of the force equilibrium. We are using thermodynamic arguments to justify this relation. So, the change in internal energy of a piezoelectric material is given by.

$$dU = \theta d\sigma + T_{jk} dS_{jk} + E_i dD_i \qquad (2.16)$$

Where θ is the temperature and σ the entropy. By introducing the thermodynamic potential, we can change the function from being defined by D_i, σ and S_{jk} to E_i, σ and S_{jk}. And this can be defined as.

$$G = U - E_i D_i \qquad (2.17)$$

And we can obtain the exact differential from equation (2.17)

$$dG = \theta d\sigma + T_{jk} dS_{jk} - D_i dE_i \qquad (2.18)$$

This leads to the relation.

$$\left(\frac{\partial T_{jk}}{\partial E_i}\right)_{\sigma,S} = -\left(\frac{\partial D_i}{\partial S_{jk}}\right)_{\sigma,E} = \left(\frac{\partial^2 G}{\partial E_i \partial S_{jk}}\right)_{\sigma} \qquad (2.19)$$

The subscripts here above are used to indicate the relevant parameters that are assumed constant under the derivation. Then by combining equation (2.14) with equation (2.19) we can obtain.

$$\left(\frac{\partial T_{jk}}{\partial E_i}\right)_{\sigma,S} = -e_{ijk} \qquad (2.20)$$

When looking at the linear region of equation (2.21) we can see that we can integrate directly here. And when combined this result with the possibility that the piezoelectric material can also experience the strain, the stress can be given with the following tensor form.

$$T_{ij} = c_{ijkl}^{E} S_{kl} - e_{kij} E_k \qquad (2.21)$$

What we have referred to here with equation (2.14) and (2.21) are the constitutive equations for linear piezoelectric theory, in a form called by some the e-form. The manipulations were the terms that will stay on the left side of the equation are given the form (g, d and h) and can be seen in Appendix A. And an overview of these relevant fields and constant with corresponding units are given in Table 6.2 in the appendix.

Now that we have defined the piezoelectric constitutive equations, we can begin to introduce Maxwell's equations. And as the elastic waves associated with the electric field travels in an order 5 times slower than the electromagnetic waves, we can use a quasi-static approximation. Leading to this relation.

$$\nabla \times E = -\frac{\partial B}{\partial t} \cong 0 \qquad (2.22)$$

Here B is the magnetic field. In this simplification the electric field will have a negative gradient to the electric potential (Φ) and can be given as.

$$E = -\nabla \Phi \qquad (2.23)$$

We will also assume that there are no free charges as the piezoelectric material behaves as a perfect insulator. This leads to the simplification of the electrical displacements as the following.

$$\nabla \cdot D = 0 \qquad (2.24)$$

And by finally combining the equations (2.1), (2.6), (2.21), (2.23) and (2.24) we can create a set of governing equations for elastic waves in a piezoelectric material in tensor form [19], [20].

$$\rho \frac{\partial^2 u_i}{\partial t^2} - c_{ijkl}^E \frac{\partial^2 u_l}{\partial x_j \partial x_k} - e_{kij} \frac{\partial^2 \Phi}{\partial x_j \partial x_k} = 0 \qquad (2.25)$$

$$e_{kij} \frac{\partial u_l}{\partial x_k} - \varepsilon_{jk}^S \frac{\partial \Phi}{\partial x_k} = 0 \qquad (2.26)$$

2.4 Tensor Transformations

Tensor calculation is a complex, but very integral part of any physical calculation and hence simulations. However, getting a good intuitive understanding of tensor calculation isn't easy. One way to try and understand this is by viewing tensors as its own set of laws, as ever basic vector and components will share the same reference frame. This makes it possible for us to change the coordinate system and the corresponding components will change accordingly. This is very useful when looking into materials where the crystal cut will impact the propagation directions. And as such the only transformation we will be interested in here will be rotation.

First, we will consider the traditional unit vector of the cartesian coordinate system. Where $\hat{\imath}$, $\hat{\jmath}$ and $\hat{k}$, represents the three directions x, y and z respectively. And any of these vectors can be mapped to any other three vectors, $\widehat{\imath'}$, $\widehat{\jmath'}$ and $\widehat{k'}$ by the 3x3 matrix $\boldsymbol{R}$ as follows.

$$\begin{bmatrix} \widehat{\imath'} \\ \widehat{\jmath'} \\ \widehat{k'} \end{bmatrix} = \begin{bmatrix} l_1 & m_1 & n_1 \\ l_2 & m_2 & n_2 \\ l_3 & m_3 & n_3 \end{bmatrix} \cdot \begin{bmatrix} \hat{\imath} \\ \hat{\jmath} \\ \hat{k} \end{bmatrix} = \boldsymbol{R} \cdot \begin{bmatrix} \hat{\imath} \\ \hat{\jmath} \\ \hat{k} \end{bmatrix} \qquad (2.27)$$

We can also perform a similar reversed mapping with $\boldsymbol{R}^{-1}$ given by.

$$\begin{bmatrix} \hat{\imath} \\ \hat{\jmath} \\ \hat{k} \end{bmatrix} = \begin{bmatrix} l_1 & m_1 & n_1 \\ l_2 & m_2 & n_2 \\ l_3 & m_3 & n_3 \end{bmatrix} \cdot \begin{bmatrix} \widehat{\imath'} \\ \widehat{\jmath'} \\ \widehat{k'} \end{bmatrix} = \mathbf{R^{-1}} \cdot \begin{bmatrix} \widehat{\imath'} \\ \widehat{\jmath'} \\ \widehat{k'} \end{bmatrix} \quad (2.28)$$

The arbitrary mapping of one set of units to another set of unit vectors can be done with the Euler's angels of three independent angels (a, b, c). However, it is important to consider which axis is being rotated and in which order. There are three common Euler conventions that we could be considered, this could be (z, x', z''), (z, y', z'') and (x, y', x'') where the rotation is being done counterclockwise to a specified axis [21]. And here on we will consider only the second convention (z, y', z''). As such the new set of unit vectors after the rotation from the first axis (z) can be given as.

$$\begin{bmatrix} \widehat{\imath'} \\ \widehat{\jmath'} \\ \widehat{k'} \end{bmatrix} = \begin{bmatrix} \cos(a) & \sin(a) & 0 \\ -\sin(a) & \cos(a) & 0 \\ 0 & 0 & 1 \end{bmatrix} \cdot \begin{bmatrix} \hat{\imath} \\ \hat{\jmath} \\ \hat{k} \end{bmatrix} \quad (2.29)$$

And rotation around the second axis (y').

$$\begin{bmatrix} \widehat{\imath''} \\ \widehat{\jmath''} \\ \widehat{k''} \end{bmatrix} = \begin{bmatrix} \cos(b) & 0 & -\sin(b) \\ 0 & 1 & 0 \\ \sin(b) & 0 & \cos(b) \end{bmatrix} \cdot \begin{bmatrix} \widehat{\imath'} \\ \widehat{\jmath'} \\ \widehat{k'} \end{bmatrix} \quad (2.30)$$

And finally, the rotation around the third axis (z'').

$$\begin{bmatrix} \widehat{\imath'''} \\ \widehat{\jmath'''} \\ \widehat{k'''} \end{bmatrix} = \begin{bmatrix} \cos(c) & \sin(c) & 0 \\ -\sin(c) & \cos(c) & 0 \\ 0 & 0 & 1 \end{bmatrix} \cdot \begin{bmatrix} \widehat{\imath''} \\ \widehat{\jmath''} \\ \widehat{k''} \end{bmatrix} \quad (2.31)$$

Now we can obtain the complete rotation matrix $\boldsymbol{R}$, this is possible to do by substituting equation (2.29) and (2.30) into equation (2.31) and performing the matrix multiplications. This will come out in the following form.

$$R = \begin{bmatrix} \cos(a)\cos(b)\cos(c) - \sin(a)\sin(c) & \cos(b)\cos(c)\sin(a) + \cos(a)\sin(c) & -\cos(c)\sin(b) \\ -\cos(a)\cos(b)\sin(c) - \cos(c)\sin(a) & -\cos(b)\sin(a)\sin(c) + \cos(a)\cos(c) & \sin(b)\sin(c) \\ \cos(a)\sin(b) & \sin(a)\sin(b) & \cos(b) \end{bmatrix} \quad (2.32)$$

The rotation matrix $\boldsymbol{R}$ in equation (2.32) is a general form and can be utilized to transform any 1st and 2nd rank tensors to any new reference frame with its new set of vectors. Now consider the relation between electric displacement ($\boldsymbol{D}$) and electric field ($\boldsymbol{E}$) with respect to the two different coordinate systems.

$$D = \varepsilon E \text{ and } D' = \varepsilon' E' \quad (2.33)$$

ε is the permittivity tensor (rank 2) and here we will leave out all the corresponding tensors indices for simplicity. D and E are both vectors and can hence be transformed using equation (2.27) ($D' = RD$ and $E' = RE$). And substituting them into the marked terms in equation (2.33) gives.

$$RD = \varepsilon' RE \quad (2.34)$$

Now by multiplying equation (2.34) with $\boldsymbol{R}^{-1}$ and by comparing the results with the unmarked terms in equation (2.33) we can obtain the transformation of ε, This leads to the following transformation of ε.

$$\varepsilon = R^{-1}\varepsilon' R \text{ and } \varepsilon' = R\varepsilon R^{-1} \quad (2.35)$$

Here we can see that the relation in equation (3.35) is a general transformation that can be applied to any 2nd rank tensor. However, it is useful to look at Voigt notation before advancing to the 3rd and 4th rank tensors. And because of the symmetry shown for stress and strain in equation (2.2) and (2.3), we can reduce the 9 total components down to only 6 independent ones. So, using Voigt notation we will map these 9 components into these 6 independent components. The relations are shown in Table 1.

Index		*Voigt*
11	→	*1*
22	→	*2*
33	→	*3*
23,32	→	*4*
13,31	→	*5*
12,21	→	*6*

Table 2.1 Voigt Notation

And since both stress and strain are a 2nd rank tensor, we can use the general 2nd rank tensor transformation defined in equation (2.35). If we rearrange the terms with respect to the 6 independent components in Voigt notations and preforming a matrix multiplication, we can then find the relation between the two different reference frames can be given by a 6x6 rotation matrix α. From here we can use α to transform any 2nd rank tensor into its Voigt notation like seen in equation (2.36) [20].

$$\begin{bmatrix} S'_1 \\ S'_2 \\ S'_3 \\ S'_4 \\ S'_5 \\ S'_6 \end{bmatrix} = \begin{bmatrix} l_1^2 & m_1^2 & n_1^2 & 2m_1n_1 & 2n_1l_1 & 2l_1m_1 \\ l_2^2 & m_2^2 & n_2^2 & 2m_2n_2 & 2n_2l_2 & 2l_2m_2 \\ l_3^2 & m_3^2 & n_3^2 & 2m_3n_3 & 2n_3l_3 & 2l_3m_3 \\ l_2l_3 & m_2m_3 & n_2n_3 & m_2n_3 + m_3n_2 & n_2l_3 + n_3l_2 & m_2l_3 + m_3l_2 \\ l_3l_1 & m_3m_1 & n_3n_1 & m_3n_1 + m_1n_3 & n_3l_1 + n_1l_3 & m_3l_1 + m_1l_3 \\ l_1l_2 & m_1m_2 & n_1n_2 & m_1n_2 + m_2n_1 & n_1l_2 + n_2l_1 & m_1l_2 + m_2l_1 \end{bmatrix} \cdot \begin{bmatrix} S_1 \\ S_2 \\ S_3 \\ S_4 \\ S_5 \\ S_6 \end{bmatrix} = \alpha \cdot \begin{bmatrix} S_1 \\ S_2 \\ S_3 \\ S_4 \\ S_5 \\ S_6 \end{bmatrix} \quad (2.36)$$

Then by following the same procedure we used to obtain the transformation relation, between the two different reference frames, for ε as done in equation (2.33), (2.34) and (2.35). It is now possible to obtain a transformation relation for the piezoelectric tensor (e) and the stiffness tensor (c). So, for a 3rd rank tensor like e we can give the transformation the following form.

$$e' = Re\alpha^{-1} and\ e = R^{-1}e'\alpha \quad (2.37)$$

And for a 4th rank tensor like c the transformation will have the form as following.

$$c' = \alpha c \alpha^{-1} \; and \; c = \alpha^{-1} c' \alpha \qquad (2.38)$$

The direction cosines $l's$, $m's$ and $n's$ given in equation (2.27) and the subscripts 1-3 defines the new axis they relate to. All these components can be obtained by the general rotation matrix equation (2.32) given by Euler angels a, b and c. In a lot of cases the change in a coordinate system is done such that the two rotation matrices R and α will be symmetric and making the invers matrices R^{-1} and α^{-1} can be changed with the corresponding transpose matrices R^T and α^T. The summarized transformation of ε, e and c can be seen in Table 2, while the general tensor transformation with full indices can be seen in Table 3.

Table 2.2 Material Transformations

Tensor	Rank	*Transformation*
Permittivity	2	$\varepsilon' = R\varepsilon R^{-1}$
Piezoelectric	3	$e' = Re\alpha^{-1}$
Stiffness	4	$c' = \alpha c \alpha^{-1}$

Equation (2.27) gives R or with Euler's angels in (2.32). while α is given in equation (2.36).

Table 2.3 Tensor Transformations

Rank	*Transformation*
1	$A_i^{'} = a_{ij} A_j$
2	$A_{ij}^{'} = a_{ik} a_{jl} A_{kl}$
3	$A_{ijk}^{'} = a_{il} a_{jm} a_{kn} A_{lmn}$
4	$A_{ijkl}^{'} = a_{im} a_{jn} a_{kp} a_{lq} A_{mnpq}$

Here Einstein summation convention are used.

2.5 Fundamental Lamb Wave Theory

Under this segment the main procedure and derivation is done with reference of "Elastic waves in Solid" [22]. To start making a usable equation for the Lamb wave frequency we first need to start with the displacement of material as a scalar potential ϕ and vector potential ψ.

$$u = \nabla\phi + \nabla \wedge \psi \qquad (2.39)$$

Here the potential must satisfy the wave equations below. Where V_L and V_T is the phase velocity in the longitudinal and transverse direction respectively.

$$\nabla^2\phi - \frac{1}{V_L^2}\frac{\partial\phi}{\partial t^2} = 0 \; and \; \nabla^2\psi - \frac{1}{V_T^2}\frac{\partial\psi}{\partial t^2} = 0 \qquad (2.40)$$

Now considering the Lamb wave propagation along the x direction, so that $\partial_3 \equiv \frac{\partial}{\partial x_3} = 0$. And in the sinusoidal case $\frac{\partial}{\partial x_1} = \partial_1 = -ik$, now the displacement components can be written in the following form.

$$u_1 = \partial_1\phi + \partial_2\psi_3 = -ik\phi + \partial_2\psi_3 \;\; and \; u_2 = \partial_2\phi + \partial_1\psi_3 = \partial_2\phi + ik\psi_3 \qquad (2.41)$$

Whereas the transverse vertical wave displacement will have the form.

$$u_3 = -(ik\psi_2 + \partial_2\psi_1) \qquad (2.42)$$

and equation (2.42) can be written in Laplacian in the following form.

$$\nabla^2 = \frac{\partial^2}{\partial x_1^2} + \frac{\partial^2}{\partial x_2^2} = -k^2 + \frac{\partial^2}{\partial x_2^2} \quad (2.43)$$

Now by defining the wave number for longitudinal and transverse waves as such.

$$p^2 = \frac{\omega^2}{V_L^2} - k^2 \; and \; q^2 = \frac{\omega^2}{V_T^2} - k^2 \quad (2.44)$$

Equation (2.44) must satisfy the equations below.

$$\partial_2^2 \phi + p^2 \phi = 0 \; and \; \partial_2^2 \psi + q^2 \psi = 0 \quad (2.45)$$

However, an acceptable solution is based on the boundary condition we set. This makes it very hard to create an accurate estimation of more advance structures. So, we will assume a very simple isotropic 2-dimensional plate. We do this to simplify the equations making them more intuitive for understanding the principals of Lamb wave. This will make the equation we find from here be less accurate for calculating variables for our Lamb Wave Resonator. And as such our boundary conditions will be set at $x_2 = \pm h$ in form.

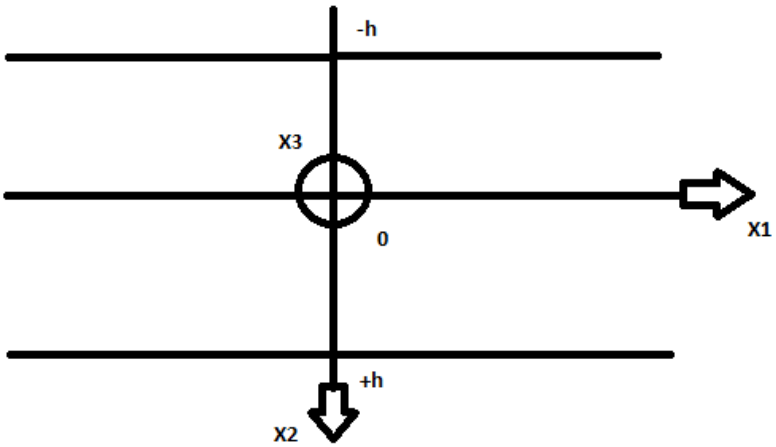

Figure 2.3 Lamb wave displacement directions

$$T_{32} = 0, T_{22} = T_2, T_{12} = T_6 \quad (2.46)$$

And at the faces will be set to be.

$$T_2 = T_6 = 0 \quad (2.47)$$

So, in a isotropic plate we can set $c_{44} = c_{66}$ and since $S_{33} = \partial_3 u_3 = 0$ the dilatation will have the form.

$$S = S_{11} + S_{22} = \partial_1 u_1 + \partial_2 u_2 = \nabla^2 \phi \quad (2.48)$$

And with the normal stress given by.

$$T_2 = c_{11}\nabla^2\phi - 2c_{66}\partial_1 u_1 = c_{11}\nabla^2\phi + 2c_{66}(k^2\phi + ik\partial_2\psi) \quad (2.49)$$

Now putting (2.40) and (2.44) into the form $\rho\omega^2 = c_{66}(k^2 + q^2)$ we can get the normal stress in the form.

$$T_2 = c_{66}[(k^2 + q^2)\phi + 2ik\partial_2\psi] \quad (2.50)$$

Given a similar approach we can get the tangential stress in the form.

$$T_6 = c_{66}[(k^2 + q^2)\psi + 2ik\partial_2\phi] \quad (2.51)$$

As the requirements for these functions $T_2 = T_6 = 0$ at $x_2 = \pm h$ make the only place that both are simultaneously satisfied being when they are odd or even. So, question (2.45) must have different parity, and so can take the form.

$$\phi = Bcos(px_2 + \alpha) \; and \; \psi = Asin(qx_2 + \alpha) \quad (2.52)$$

Where $\alpha = 0$ for (T_2 even, T_6 odd) and $\alpha = \pi/2$ for (T_2 odd, T_6 even), note we have omitted the propagation factor of exp$[i(\omega t - kx_1)]$. Now my using (2.41) we can get the mechanical displacements in the form.

$$u_1 = -ikBcos(px_2 + \alpha) + qAcos(qx_2 + \alpha) \text{ and } u_2 = -pBsin(px_2 - \alpha) + ikAsin(qx_2 + \alpha) \quad (2.53)$$

Now we can see that we have two types of Lamb wave, this being the symmetric ($\alpha = 0$) and antisymmetric ($\alpha = \pi/2$) modes. And when setting α to one of these modes the boundary condition will yield these two equations.

$$(k^2 - q^2)Bcos(ph + \alpha) + 2ikqAcos(qh + \alpha) = 0 \quad (2.54)$$

$$2ikpBsin(ph + \alpha) + (k^2 - q^2)Asin(qh + \alpha) = 0 \quad (2.55)$$

Now by adding (2.54) and (2.55) to each other we can dispersion relation between ω and k called the Rayleigh-Lamb equation in the form were $\alpha = 0$ or $\pi/2$.

$$\frac{\omega^4}{V_T^4} = 4k^2q^2[1 - \frac{p}{q}\frac{tan\,(ph + \alpha)}{tan\,(qh + \alpha)}] \quad (2.56)$$

To create a more analytical and workable solution of equation (2.56) we need to investigate the (ω, k) plane. As here three distinct planes can be separated form each other, these three depending on if the phase velocity $V = \omega/k$ exceeds the longitudinal phase velocity $V_L = (c_{11}/\rho)^{1/2}$ or the transverse phase velocity $V_T = (c_{66}/\rho)^{1/2}$. So hence we can rewrite equation (2.44) into the forms.

$$p^2 = \omega^2(\frac{1}{V_L^2} - \frac{1}{V^2})\ and\ q^2 = \omega^2(\frac{1}{V_T^2} - \frac{1}{V^2}) \quad (2.57)$$

However, in this project we are only interested in the first case were both the wavenumbers are real. So, we can write that.

$$V > V_L > V_T\ or\ k < \omega/V_L < \omega/V_T \quad (2.58)$$

Now we can rewrite equation (2.56) for modes without a cut-off frequency as the following form.

$$\frac{\omega^4}{V_T^4} \cong 4k^2(q^2 - p^2) = 4k^2\omega^2(\frac{1}{V_T^2} - \frac{1}{V_L^2}) \quad (2.59)$$

This shows that the phase velocity tends to a finite limit called the plate velocity.

$$V_p = V_L\sqrt{1 - \frac{c_{12}^2}{c_{11}^2}} \quad (2.60)$$

Now taking equation 2.59 we can rewrite it as

$$\omega = 2k\sqrt{\frac{V_L^2V_T^2 - V_T^4}{V_L^2}} \quad (2.61)$$

Lastly by using equation 2.61 and adding it into $f = \frac{v}{\lambda}$ and $v = \frac{\omega}{k}$ we can get an approximation for the S0 frequency response in an ideal plate.

$$f_{S0} = \frac{2}{\lambda}\sqrt{\frac{V_L^2V_T^2 - V_T^4}{V_L^2}} \quad (2.62)$$

However, for the second device we will not be interested in the 0-order symmetric (S0) mode of Lamb wave. But rather the 0-order horizontal symmetrical (SH0) mode. And to find a simple approximation for the frequency at which this mode occurs we will again do some of the same assumptions we did about the S0 mode. So, we will again assume a simple isotropic material instead of the piezoelectrical material used in the main. We will also assume similar boundary conditions with a perfect infinite plate. To tart we can write that T_{12} and T_{22} can be seen as zero, while we will only be concerning ourselves with T_{32} and can written as

$$T_{32} = -jk(c_{45}^{E}u_3 + e_{14}u_{14}) + \frac{\partial}{\partial x_2}(c_{44}u_3 + e_{24}u_4) \quad (2.63)$$

And with substituting $\chi_2 = kx_2$, $V = \frac{\omega}{k}$ and $V_T^2 = \sqrt{\frac{c_{44}}{\rho}}$ into T_{32} and using the same isotropic simplification as done previously we can write.

$$\frac{\partial^2 u}{\partial x_2^2} + \left(\frac{\omega^2}{V_T^2} - k^2\right)u = 0 \quad (2.64)$$

Now, by assuming a simplified the system as a parallel-sided plate we can write the displacement as a sinusoidal in the form.

$$u(x_2) = u_0 \cos\left[\frac{n\pi}{h}(x_2 + h)\right], n = 0,1,2 \ldots \quad (2.65)$$

Simplifying this again by substituting 2.65 into 2.64 and assuming the 0-order, we can find a rough estimation for the SH0 mode a plate written as.

$$f_{SH0} = \frac{V_T}{\lambda} \quad (2.66)$$

So, the SH0 mode will mainly be determined by the material and wavelength of the device. In contrast the S0 frequency that is mainly determined by the height and wavelength of the device.
It is important to note that both equation 2.62 and 2.66 are very rough approximation. As they both assume an isotropic material condition and an ideal infinite plate. When using them to calculate the frequency response of the S0 and SH0 mode we would get 576MHz and 1085MHz respectively.

2.6 Bloch Waves

Bloch waves in crystal is another core part of this study and can also be somewhat difficult to get a natural comprehension on its principles. However, understanding its ramifications isn't too difficult

to understand. As there are two main part you can assume to make understanding this theorem better. One is that in this case crystal is just referring to any material with a rigid atomic structure, and two that when talking amount waves in crystals any single relative wave will have no idea where in the structure it is if considered the structure properly. So, starting with the assumption that that the wave equation can be written as the following form.

$$|\psi(x)|^2 = |\psi(x+a)|^2 \; and \; \psi(x+a) = C * \psi(x) = e^{jkx}\psi(x) \qquad (2.67)$$

Here a is referring to the distance between the atoms and k is an arbitrary constant that refers to the structure of the crystal called the crystal momentum. And assuming a near infinite line we assume a circular structure like in the figure below and can write that.

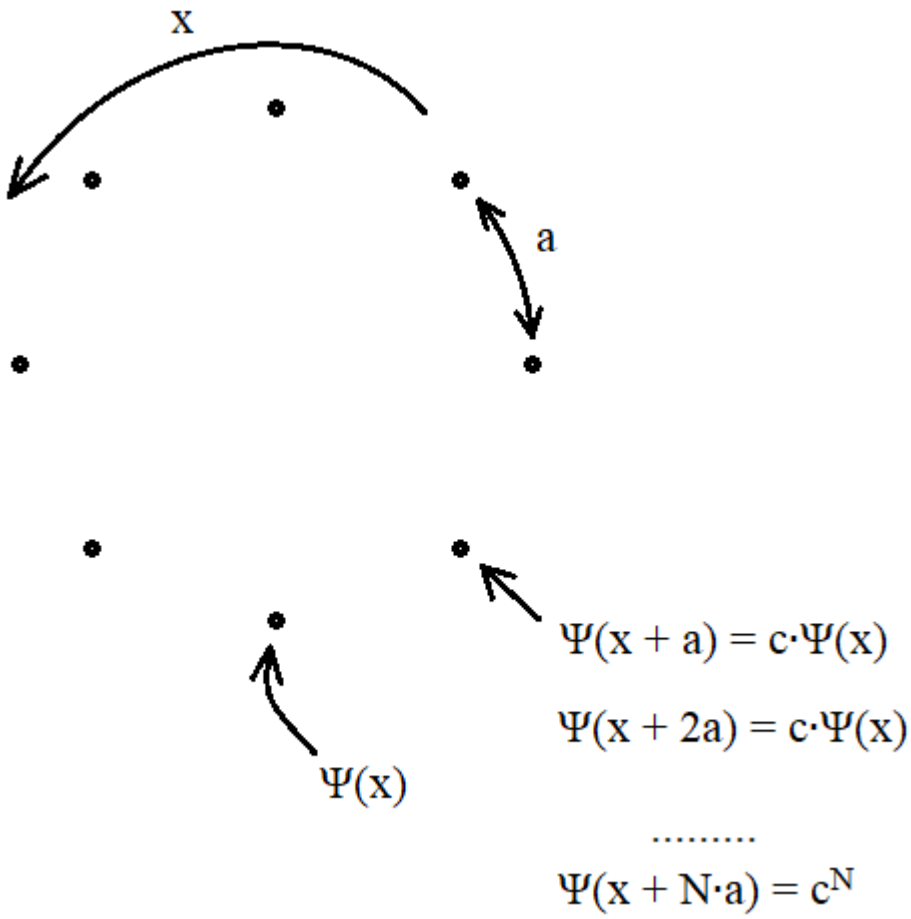

Figure 2.4 Illustration of Bloch waves in a crystal structure

$$C^n * \psi(x) = \psi(x) \quad (2.68)$$

Going from this by giving k a new index we can write the wave equation into the following form [23].

$$\psi(x) = e^{j2\pi\frac{S\,x}{Na}} = e^{jkx}u_k(x) \quad (2.69)$$

So, by finding k we can calculate every possible movement of a wave in a crystal. And we can find the equation for k if we can reduce a structure into its irreducible Brillouin zone and looking for symmetries for possible paths the wave can take.

2.7 Mesh Convergence

The last theory that will be mentioned under this section is not as complicated as the rest. It is however, arguably the most pivotal for a proper result when using a FEM method to test the viability of a concept. And this is the Mesh Convergence Study (MCS), as without understanding the MCS there is no way to know if the results of the FEM study are a close approximation of real life, or if even the results are only possible cause the improper use of a mesh gives wrong output values. In doing a MCS it is important to know the two main ways one can increase the mesh refinements. This comes in the form of h-refinement and p-refinement as seen in the figure below, the former being an increase in order of the element and the latter being a reduction in element size [24].

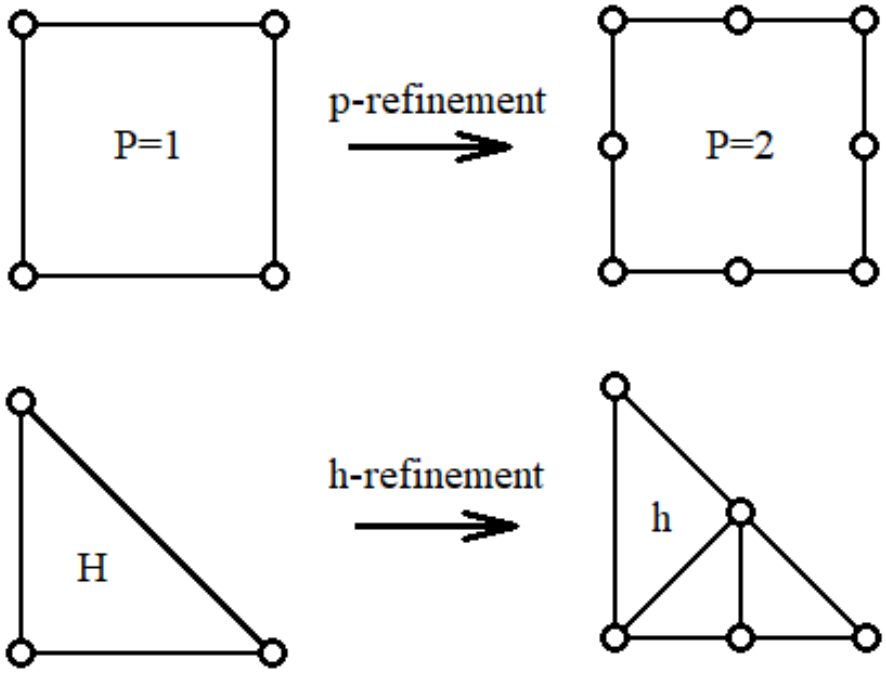

Figure 2.5 Illustration of two different forms of refinements

When doing an MCS it is important to check for changes in the results with changes in both an h and p refinements. However, in this study it is only possible to change the h-refinement. These stems from the fact that in a 3D COMSOL simulation every edge of a mesh needs to be connected to another edge of an adjacent mesh. Without this the COMSOL will refuse to run as it will have what it perceives as empty void inside the set boundaries. So later in this report we will have investigated the changes in h-refinement will have on the FEM output and look for where the results begin to converge around.

3 Modelling Methods

As mentioned previously in this thesis we have opted to use COMSOL simulation for our FEM simulation too perform our tests. However, there are different simulations needing to be made and different steps for each of these simulations needing to be followed. This is so we can be able to make sure our FEM simulation can give realistic results, for it to be able to predict realistic behaviour in a real LWR device.

So, to get our desired simulations we need to create three separate simulations. These being a small FEM simulation to find the band gap of a PCS cell. The second being a test for the relative displacement over bridge design with and without a PCS array found in the PCS simulation. Lastly one for the LWR device, this being used for the main test of the quality factor changes by the PCS array.

To create these simulations, we will need to go through different steps. Firstly, we will create a barebone simulations with the assumed required boundary conditions. Following this different test will be set up in these simulations to get an idea of the functionality of the FEM simulation. Then when the simulations are giving results corelating with what we can be expected based on other previously done studies into LWR devices, we will go into refining the simulation by finding the mesh convergence of the simulation. This step is a crucial and if this changes the result in unpredicted manners, we will have to go back and change the boundary conditions again. However, if this are set up correctly, we should see the results converge with a finer mesh. After this is done, we can proceed to change the properties of simulation to fit the different devices tested for.

3.1 Phononic Crystal Structure Band Gap

The first FEM simulation created using COMSOL for this project is a band gap simulation of a PCS cell. This simulation requires relatively simple boundary setting, as it as both a simple geometrical shape and requires very few physical boundary conditions. In the table below is starting geometrical parameters used, where the hight and radius of the slab can change depending on the desired bandgap and centre frequency needed by a LWR device.

Table 3.1 Geometrical Properties Used Before Optimization

Parameter	*AlN PCS Cell*	*$LiNbO_3$ PCS Cell*
lattice constant (a)	4 µm	0.8 µm
Slab Radius (S_R)	±1.5 µm	±0.3 µm
Slab Height (S_H)	±1 µm	±0.4 µm
Piezoelectric Layer Thickness (PL_T)	1 µm	0.3 µm
Metallic Layer Thickness (ML_T)	0.1 µm	0.1 µm

For the physic engine the inbuilt solid mechanics in COMSOL was used, where the boundary conditions is simply defining the relevant components to be piezoelectric material and setting a simple periodic conditions along the side of the substrate in the x and y directions of the simulation. As for the study done for the simulation it is an inbuild COMSOL eigenfrequency sweep study of the first 20 eigenfrequency starting at 0Hz. And then a parametric sweep where the periodic conditions are swept based on the irreducible Brillouin zone of the PCS in the simulation.

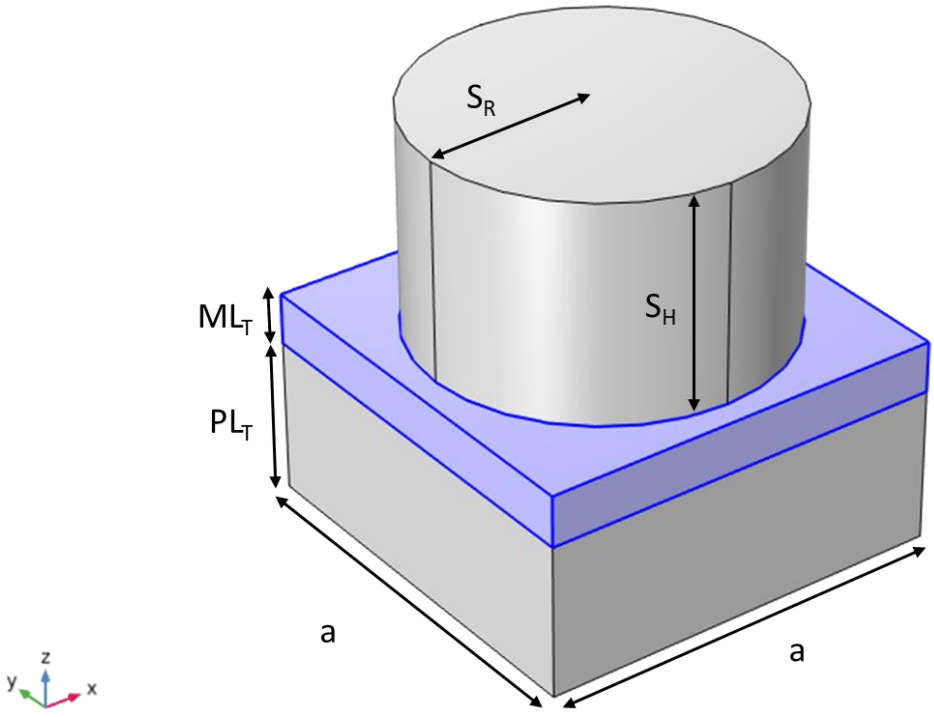

Figure 3.1 Overview of The PCS Cell Design

The above image is of an PCS cell in COMSOL, where the bottom part is where the piezoelectric boundary conditions are set. While the small plate on top of it is the metallic made of aluminium layer and it will be using a linear elastic material condition, this is also true for the metallic slab on top made of a different material. And cause of the heavy symmetry of the structure it is possibly create the irreducible Brillouin zone from the top view of the cell unit as in in the figure below.

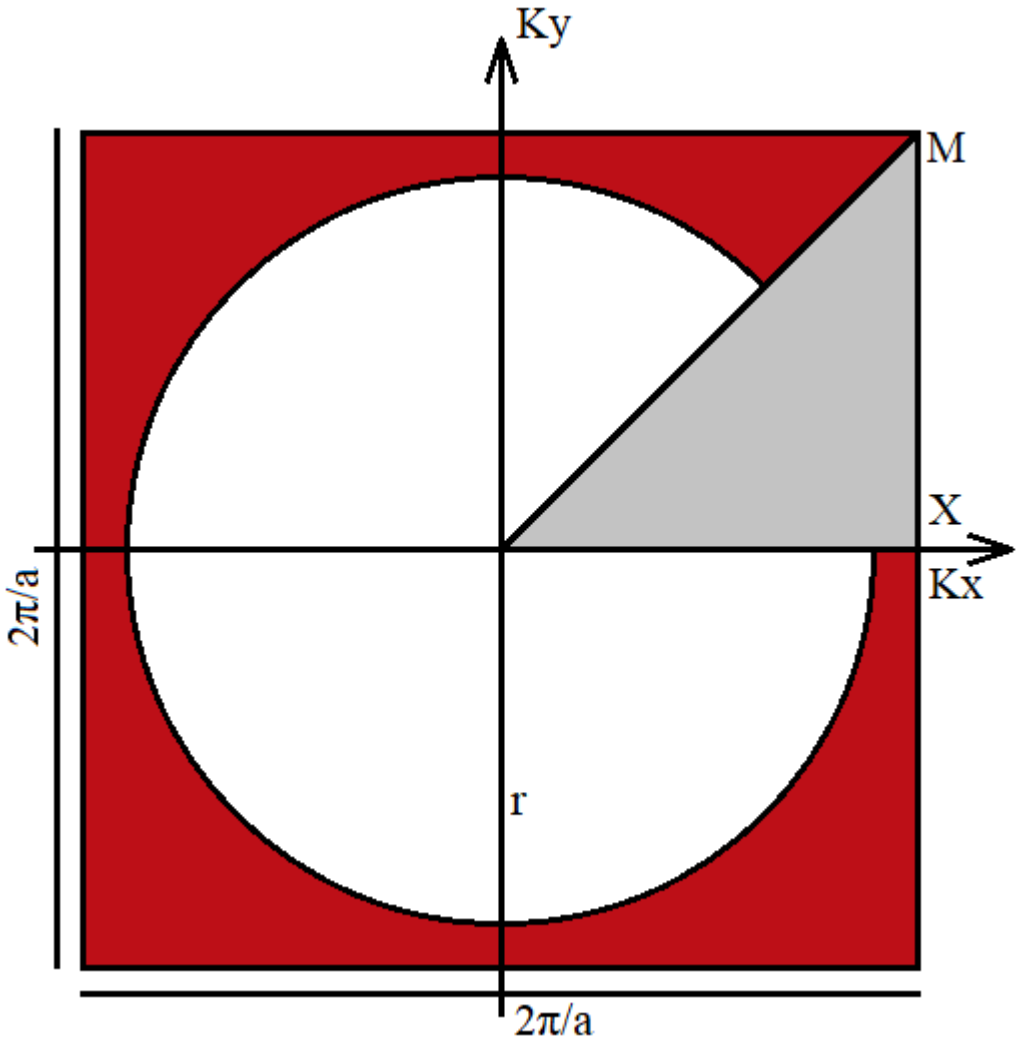

Figure 3.2 Bird's Eye View of A PCS Cell

As given in equation (2.7) we can see the general form for propagation of acoustic waves in a solid. And with the use of equation (2.65) for the relation between the wave number k and the frequency ω, given by the Bloch wave theorem. By sweeping the path $\Gamma \rightarrow \mathrm{X} \rightarrow \mathrm{M} \rightarrow \Gamma$ defined by the irreducible Brillouin zone defined as $\Gamma(0,0)$, $\mathrm{X}\left(\frac{\pi}{a},0\right)$ and $\mathrm{M}\left(\frac{\pi}{a},\frac{\pi}{a}\right)$. So, using this we can define Kx and Ky for the use in the periodic condition in the simulation. Were we will define the lattice constant as a. This will make the X component of the wave vector be $Kx = if(k < 1, k\frac{\pi}{a}, if\left(k < 2, \frac{\pi}{a}, (3-k)\frac{\pi}{a}\right))$ and the Y component of the wave vector will be $Ky = if(k < 1, 0, if\left(k < 2, (k-1)\frac{\pi}{a}, (3-k)\frac{\pi}{a}\right))$. With how the PCS simulation is set up we can find the band gap of the whole PCS cell or one of the layers individually by applying the periodic boundary conditions to both or only one of the substrate layers. Whereas the PCS cell bandgap will mainly be

defined by the bandgap of the piezoelectric layer, the lack of a band gap over a region in the metallic layer will reduce the effect of a non-infinite system.

3.2 Structural Displacement Over a Bridge Section

The second FEM simulation made is a bridge displacement transmission study. As it is very convenient to be able to show the relative reduction of displacement over a set frequency. This is both to get concrete data showing the effect of the PCS array and as a test for the functionality of the PCS array with a non-infinite array. This simulation will also only require a very simple boundary condition. As in similarity to the PCS simulation only the in-built solid mechanics engine of COMSOL will be used. Were the bottom layer of the substrate will be set as a piezoelectric material and the slabs and metallic layer will be defined as linear elastic material as seen in the figure below. We will also define port 1 with a predefined displacement in the x direction with an arbitrary but reasonable amount. As for one set of parameters used in the AIN LWR, can be seen in the table below. Where the PCS slab parameters will be matched with the optimized PCS cell parameters designed for the LWR device simulation.

Table 3.2 Properties Used in the Bridge Simulation

Parameter	*AIN Bridge*	*$LiNbO_3$ Bridge*
Piezoelectric Layer Thickness (PL_T)	1 µm	0.3 µm
Metallic Layer Thickness (ML_T)	0.1 µm	0.1 µm
Array Width	4	4
Array Length	6	3
Slab Radius (S_R)	±1.5 µm	±0.3 µm
Slab Height (S_H)	±1 µm	±0.4 µm
Cell Side Length (CS_L)	4 µm	0.8 µm
Bridge Width (B_W)	16 µm	3.2 µm
Bridge Device Length (BD_L)	56 µm	7.2 µm
PML layer length (PL_L)	8 µm	1.6 µm
Predefined Displacement	0.1 µm	0.1 µm

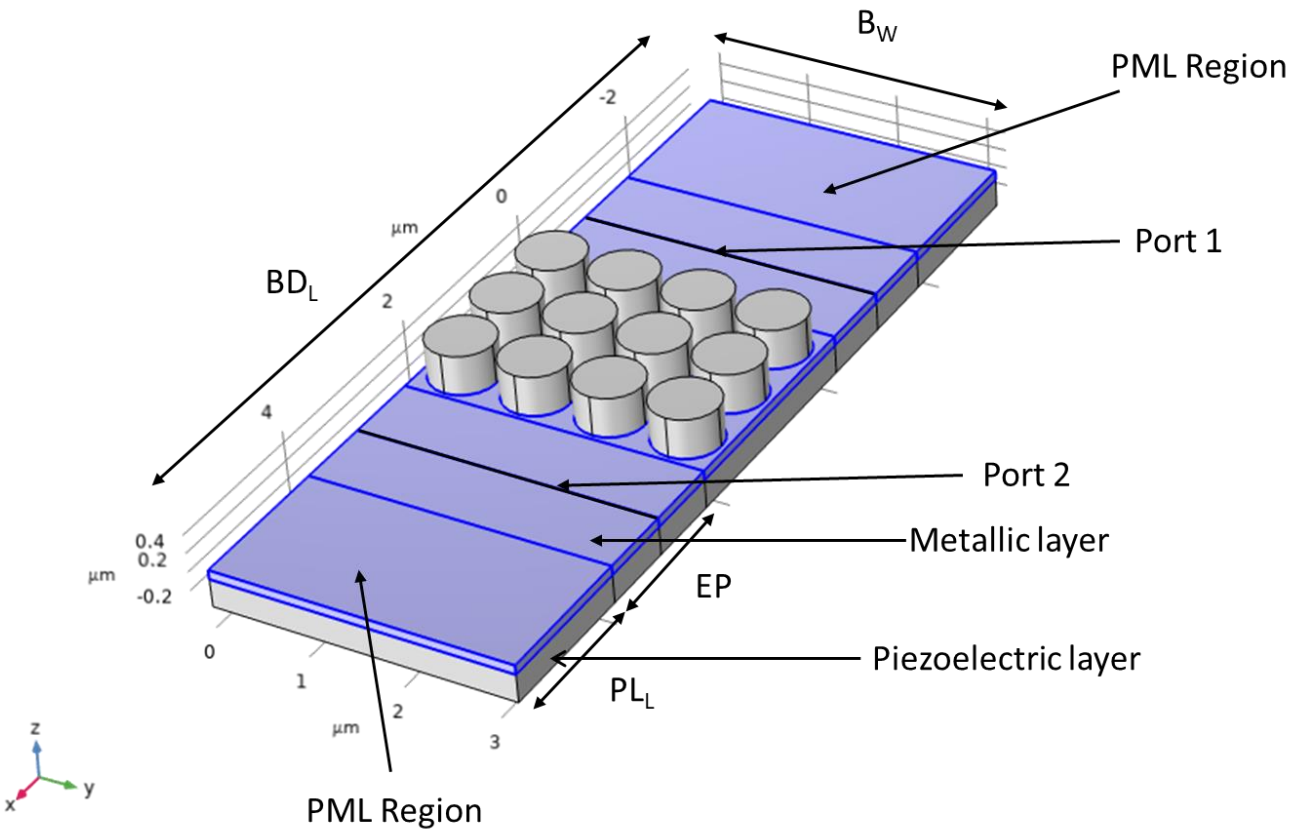

Figure 3.3 Overview of a $LiNbO_3$ Bridge Simulation Design

Next it is important to define a boundary condition on the two ends of the bridge sections as here we need to have a low reflection or absorption boundary layer, as both ends should ideally be connected to an absorbing substrate or be absorbed back into the LWR device. This can be done in some different ways. One way can be to define a low reflection boundary layer or absorption boundary layer at the ends of the bridge with the COMSOL predefined solid mechanic engine. However, we have opted into using a perfectly matched layer (PML) domain instead, as this offers a bigger freedom for geometrical shape and size of the absorption region in comparison to the two other methods. The study was done with an in-built COMSOL frequency response study with a sweep over relevant region. Then we will look at the relative change in displacement at one end of the bridge (port 1) in comparison to the predefined displacement set at the other end of the bridge structure (port 2) seen in figure above using equation 3.1.

$$S_{21} = 10 * log_{10}\left(\frac{P2}{P1}\right) = 10 * log_{10}\left(\frac{d^2_{receiving}}{d^2_{source}}\right)(dB) \quad (3.1)$$

3.3 Lamb Wave Resonator Device

The last FEM simulation is split into two different designs for the two different LWR device that is being investigated. These simulations are a fair bit more complicated in comparison to the two previously mentioned simulation. However, it does use all the principles used in them, but with some more boundary conditions also needing to be set for the electrical properties needed for the simulation. They are also somewhat different in design, as the AIN LWR simulation uses a small bridge connected to a absorbing substrate. The $LiNbO_3$ LWR uses a bridge covering the two ends of the design, with a simple absorbing boundary on the other side. It will also include a continuous and finite design simulation. So, in total there will a continuous $LiNbO_3$ LWR design and finite AIN and $LiNbO_3$ design. All designs can be seen in the figures below.

The AIN LWR device consists of a main bulk of piezoelectric materials with a small metallic layer on top like in the bridge simulation. However, this metallic layer is etched in in a combe patter forming the IDT layout over the main substrate of the device. This can be seen in the picture below of the AIN LWR device, with the parameters used for the two different devices can also be seen in the table below.

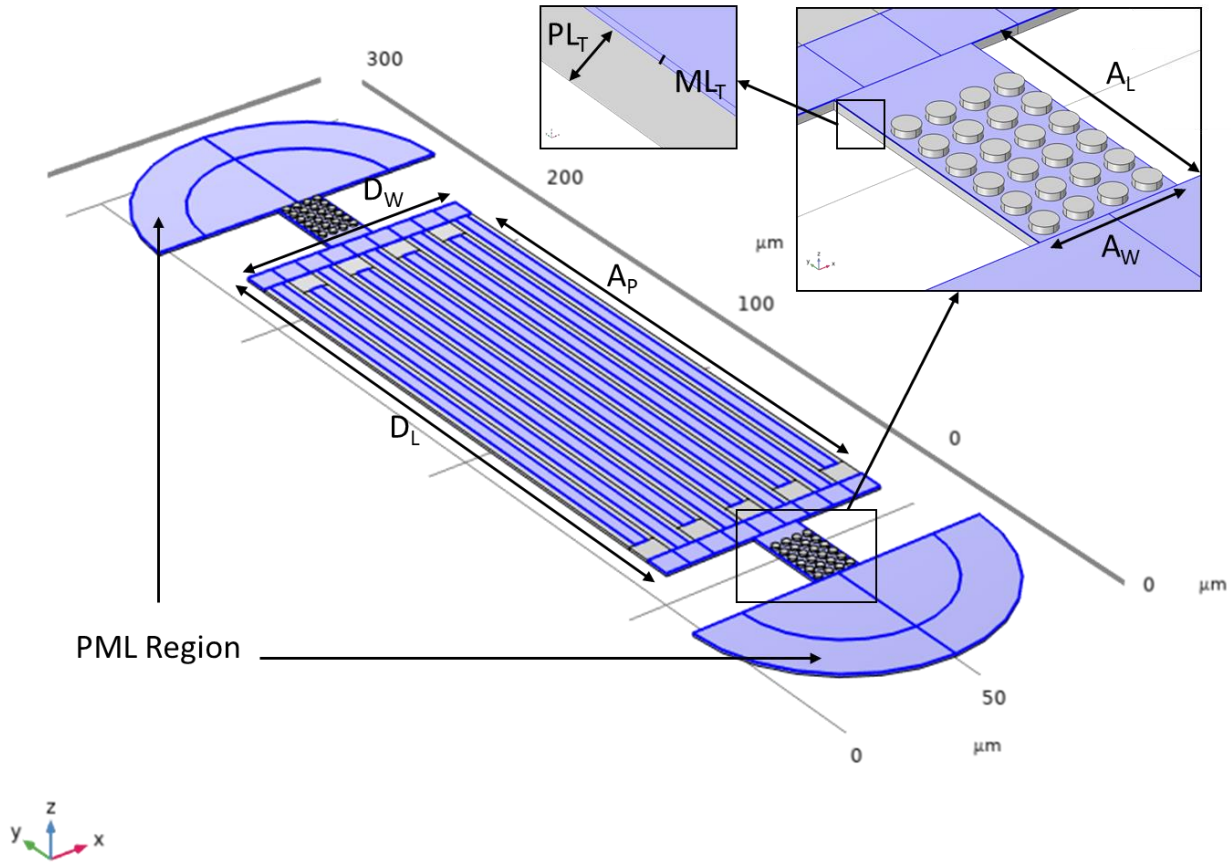

Figure 3.4 Overview of The AIN LWR Device Design

Table 3.3 Geometrical properties of LWR device's

Parameter	*AIN LWR Device*	*$LiNbO_3$ LWR device*
Electrode Pitch (Ep)	9 µm	1.6 µm
Interdigital Transducer (IDT) Finger	9	2 Continuous, 16 finite
Metallic Ratio (M_R)	0.5	0.3
Aperture (A_P)	180 µm	54.4 µm
Device Length (D_L)	216 µm	60.8 µm
Device Width (D_W)	81 µm	3.2 µm and 25.6 µm
Anchor Length (A_L)	30 µm (7.5* PCS cell size)	1.6 µm
Anchor Width (A_W)	16 µm (4*PCS cell size)	3.2 µm and 25.6 µm
PCS Array Size (x and y)	4x6	4x3
Slab Radius (S_R)	±1.5 µm	±0.3 µm

Slab Height (S_H)	±1 µm	±0.4µm
Cell Side Length (CS_L)	4 µm	0.8 µm
Piezoelectric layer thickness (PL_T)	1 µm	0.3 µm
Metallic layer thickness (ML_T)	0.1 µm	0.1 µm
Isotropic loss factor (1/Q)	1/40000	1/1000

As for the absorption substrate for the device is connected using a small bridge section. For the properties of the absorbing substrate would ideally be an infinitely large non reflective substrate. However, as a real device does not work in ideals, we assume some reflections. So, we had to design a absorption substrate with this in mind. To achieve this, we designed a two-dimensional substrate with a absorption boundary at the outer edge, letting the wave be reflected in outer plate before hitting a slow absorption boundary. So, an expanding half circle away from the device was designed. Where the radius of the first sections is 2λ and the second radius of λ on top of the last section as seen in the figure below. And to create this slow absorption region a PML layer was used for the same reasons we had in the bridge simulation.

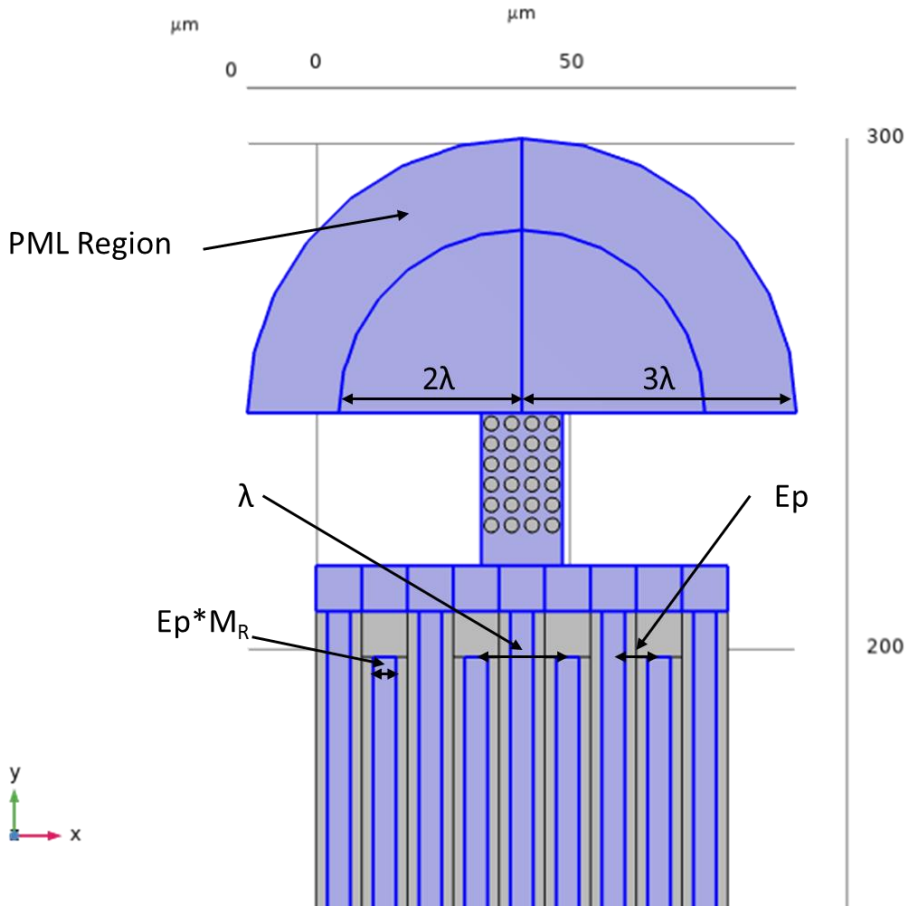

Figure 3.5 Bird's eye view of the bridge section of the AIN LWR device

The outer support region was designated as a PML region, like mentioned in the previous sections, this could have been done with a low reflection or absorption boundary conditions. However, using a PML layer allows us to have a more control of the absorption region, letting us create a large absorbing region. As for the physics engines used in this simulation, we will once again use the in-built COMSOL solid mechanics engine. Here we will connect this with a multi physics engine in COMSOL called piezoelectric effect. This will create a coupling interface between the solid mechanics engine and the last COMSOL engine used, electrostatic physic engine. Letting us simulate the effect from one on the other.

So, now the proper boundary condition settings for the device will need to be defined. Starting with the solid mechanics engine the metallic layer and the slabs will be defined as a linear elastic material, while the piezoelectrical material will be defined as such using the appropriate boundary conditions. We have also given it an isotropic loss factor of 1/Q in both the linear and piezoelectric material. Where Q will be set to 40000 in the AIN LWR device in reference to Yinjie Tong and Tao Han. [18] In contrast we will set Q to only 1000 in the $LiNbO_3$ simulation, as the value of Q was

measured to be around 1000 in our collaborators $LiNbO_3$ device [5]. As for the boundary conditions set in the electrostatic physic engine. The main function of this physic engine is simply to simulate an input terminal and ground for the system. So, here the metallic layer on upper side will be defined as a terminal with an 1V output and the other sides metallic layer as the ground.

These are all the boundary condition used for the AIN LWR device simulation. However, as mentioned the $LiNbO_3$ device will be set up slightly different. This is to reduce the simulation time, as this device we are using a long bridge follow the device width. So, a finite simulation will have a large number of mesh elements in a set distance. Making the simulation time many times longer than any of the previously done simulations.

It is also important to note that the SH0 wave propagates parallel to the plate in contrast to the S0 mode. So, the outer section would see no noticeable refractions of the wave in contrast to the S0 mode waves. Hence, the simplified absorption boundary to reduce simulation elements.

The $LiNbO_3$ device simulations will be made up of two different simulations. One simulation of a set of 2 IDT where the sides of the simulation will be set as a continues periodic boundary condition. This would give us the possibility to quickly simulate an ideal infinite device. The second simulation will be a finite device size as in the AIN LWR device. However, here the device will be 8 sets of 2 IDT in contrast to the AIN devices 9 IDT non symmetrical setup. The two different setups for the $LiNbO_3$ devices can be seen in the figure below.

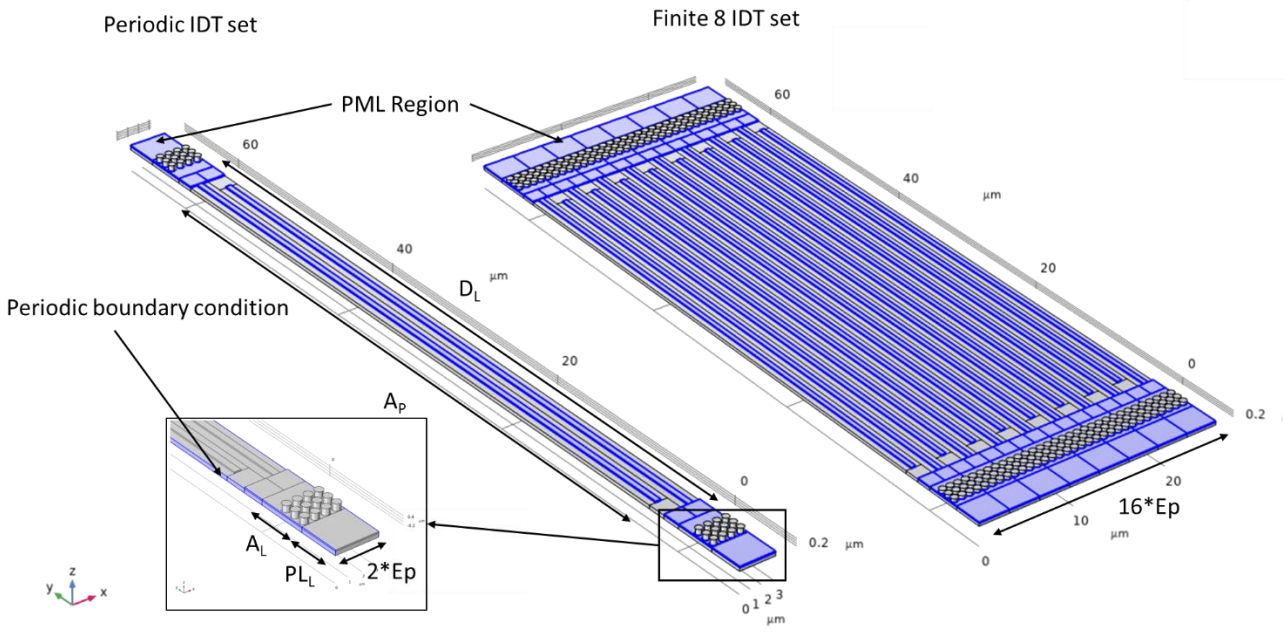

Figure 3.6 $LiNbO_3$ periodic device simulation, blue region representing the metallic layer

In the end a similar study will be done on all the different LWR device simulation setups. Where a frequency study will be done on the system. Letting us see the admittance of the system over a studied frequency range.

3.4 Mesh Convergence Study

Before any of the FML models can be of use however, a mesh convergence study will have to be done on each of the three simulation models. However, optimizing the mesh of a FEM model is a tedious and slow process. This comes from the fact that we have three separate dimensions we can get an increase in the h-refinement on the FEM model. This is true for each separate region of the FEM model, making it a very time-consuming process if one wants to optimize the mesh for both a functional result and a reasonable simulation time.

For the simpler simulations we can simply reuse the mesh found for the LWR device model or use a very fine mesh as these simulations are not vey time consuming in the first place. However, for the LWR device FEM model having an optimized mesh can make the difference between having a 60-hour simulation time or having a 500-hour simulation time.

In the LWR model we have three different sweeps for the h-refinement on the main device and a simpler two directional increase on the bridge and substrate part of the simulation. On the main device segment of the model, we can increase the h-refinement in the length, width, and thickness direction of the model. However, because of how the boundaries are designed in this simulation the minimum h-refinement will be 1 element over the electronic pitch in the length of the device increasing by x element in this boundary where x is a positive integer. And along the width of the device the minimum element size of the mesh is 4 element per electronic pitch, increasing with 4x elements where x is a positive integer again. And along the thickness the minimum element size is just the thickness of each segment of the model. As for the outer section of the device consisting of the bridge and anchor segment its mesh size is defined as a prerendered triangle field generated by COMSOL, here the maximum element size will be defined as the electron pitch divide by x elements. This effectively lets us set how many elements we want in the x and y direction of the model in this region. This can be seen in the figure below, where the left shows a low longitudinal refinement and the right showing a high refinement in the longitudinal direction.

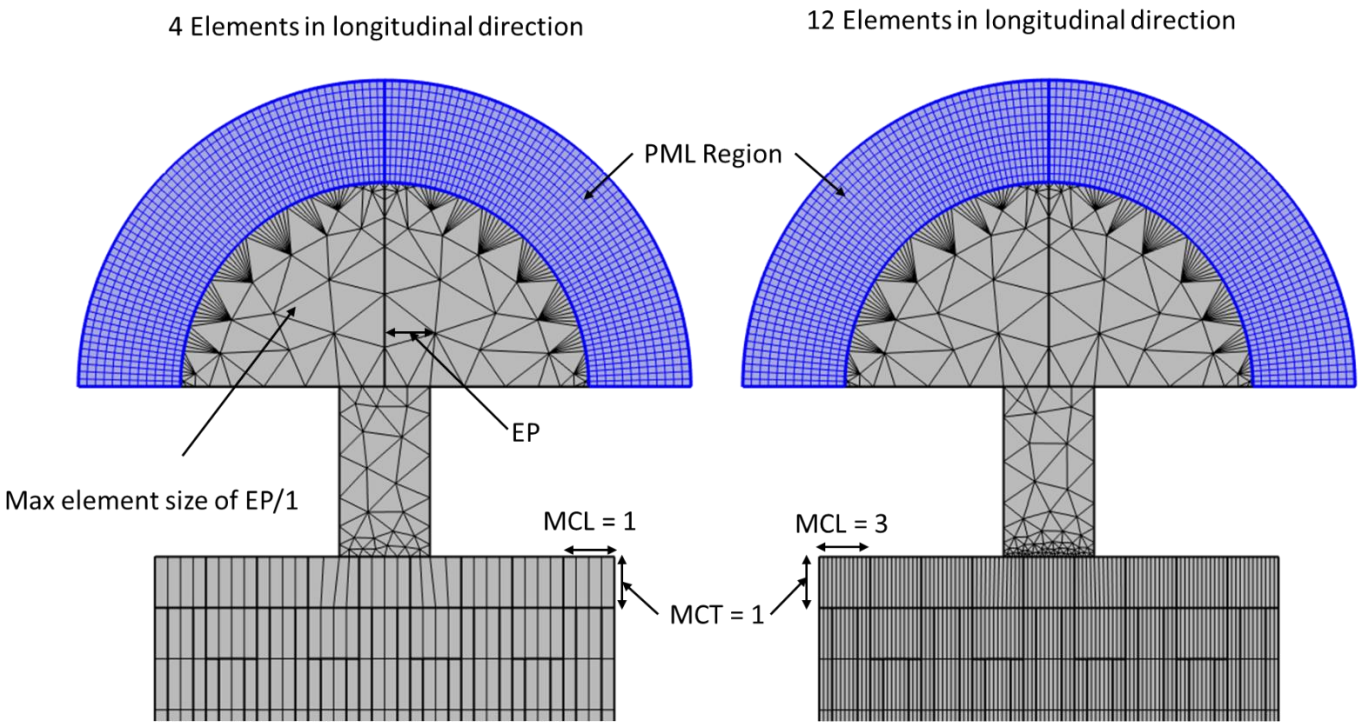

Figure 3.7 Overview of some potential mesh refinement on an AIN LWR device

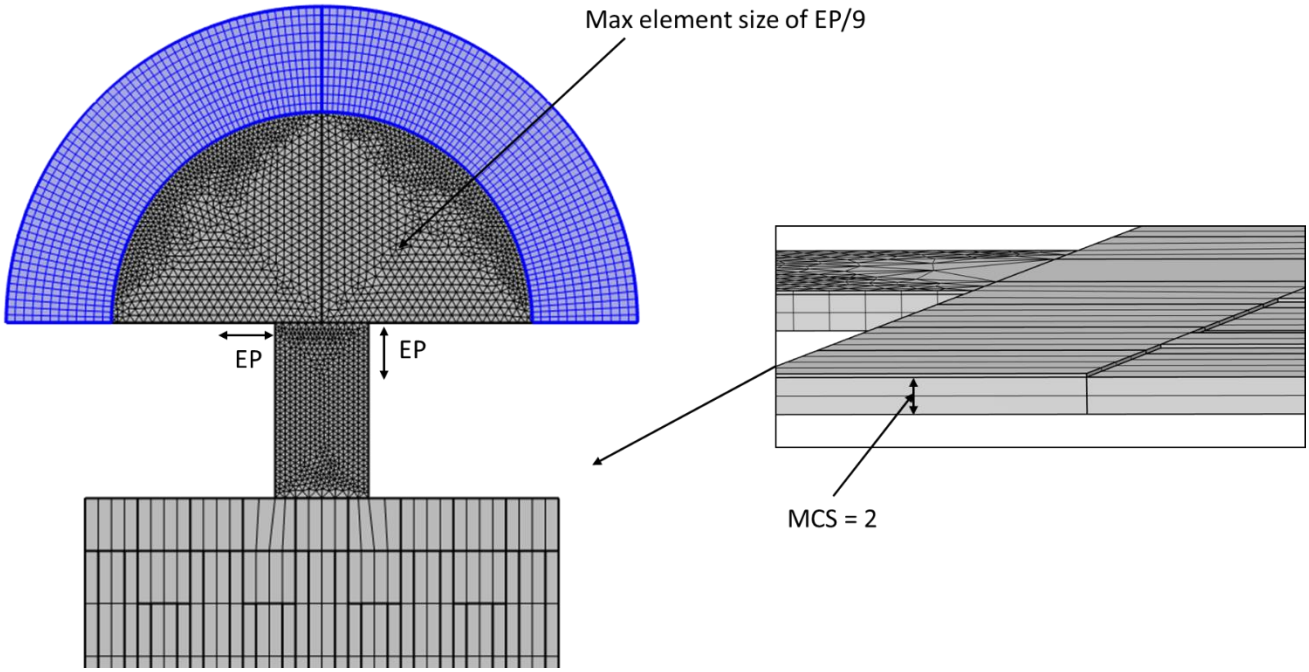

Figure 3.8 Overview of a small mesh element size on the bridge section and the mesh element size over the thickness of the device

With all of this set up we can perform the mesh convergence study on the LWR FEM model. The Mesh convergence of the one AIN LWR simulation can be seen in the different pictures below. This was done with some previously used AIN LWR device parameters, so its frequency response is different than the result of later devices. This does not change the validity of the found mesh, and the same mesh will be used for the $LiNbO_3$ LWR device. As both device's functions with similar principles, a similar mesh configuration should suffice, reducing the need for a second mesh convergence study and saving hours of simulation time. Note that in these graphs MCS refers to the refinement over the thickness of the device, not the mesh convergence study.

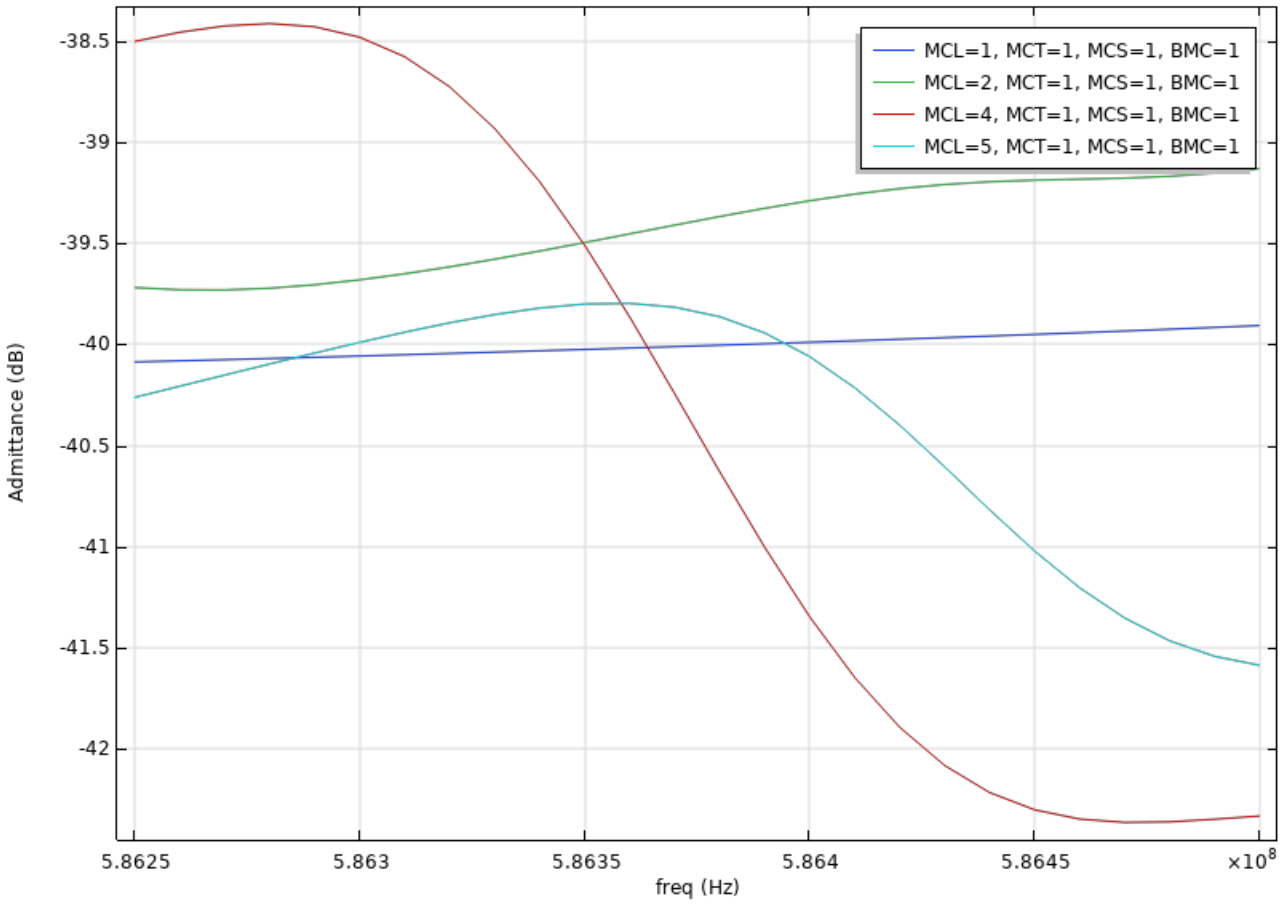

Figure 3.9 Anti resonance peaks of an old AIN LWR simulation longitudinal refinement change, low refinement in other directions

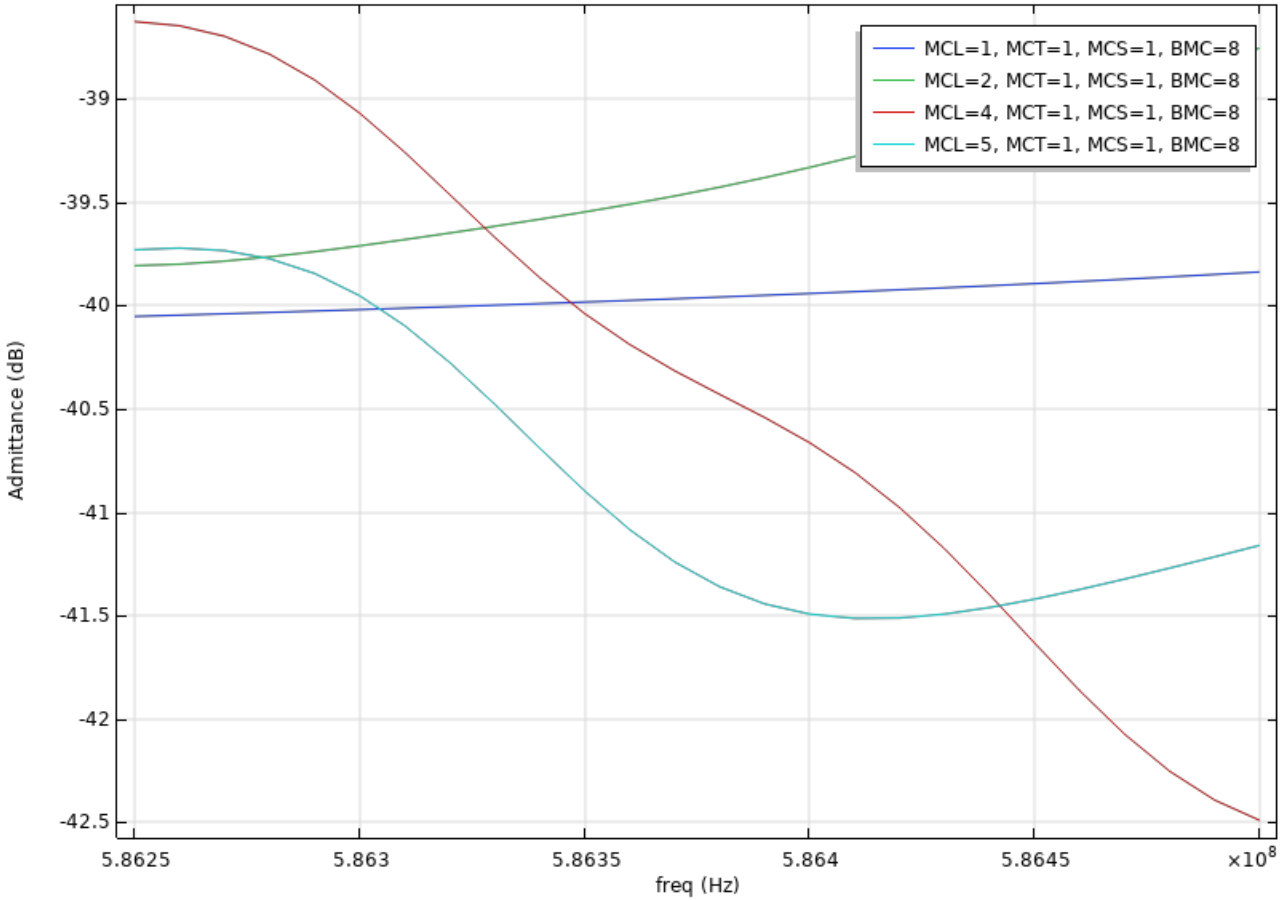

Figure 3.10 Anti resonance peaks of an old AIN LWR simulation longitudinal refinement change, low refinement in other directions, high bridge mesh refinement

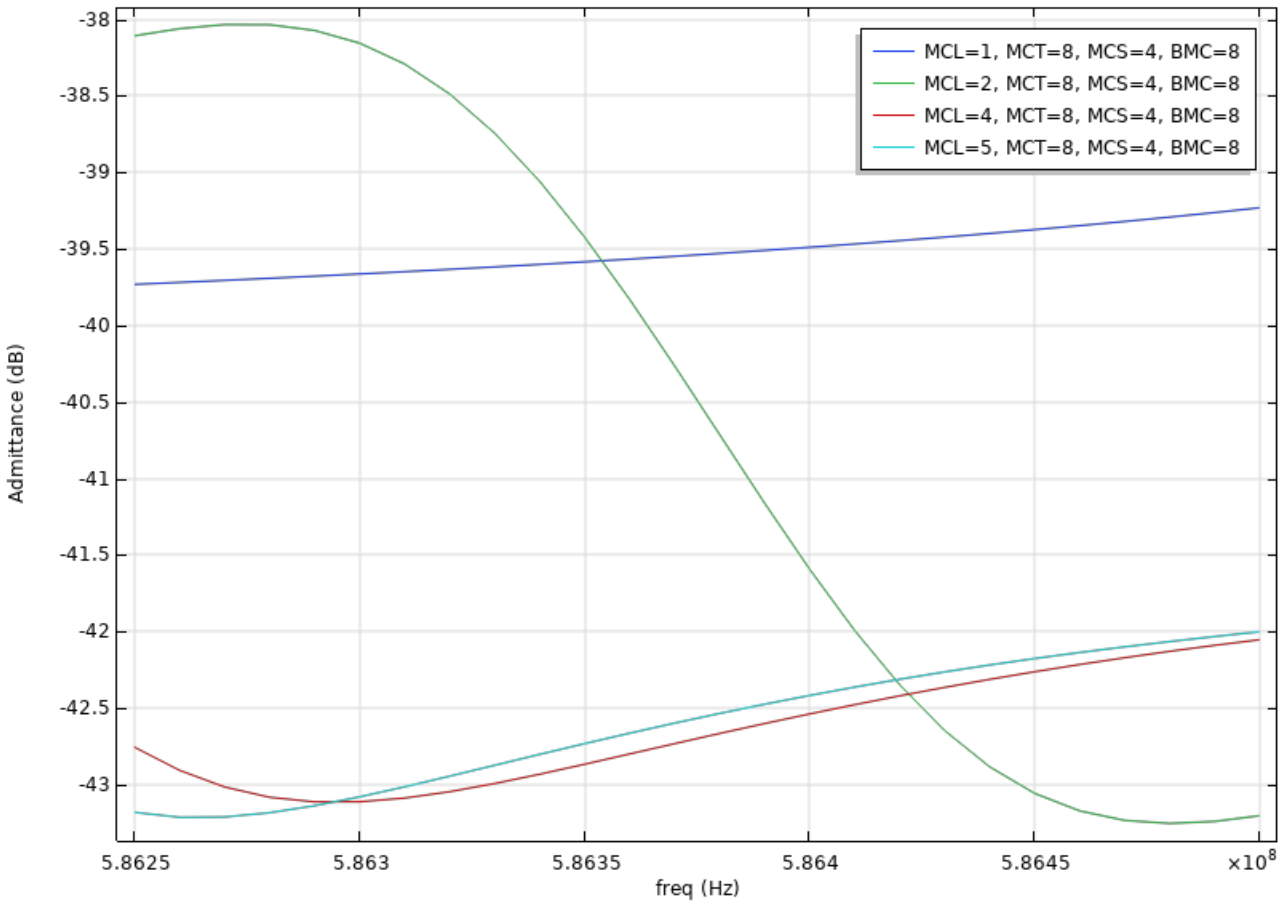

Figure 3.11 Anti resonance peaks of an old AIN LWR simulation longitudinal refinement change, high refinement in other directions

Here the three above graphs include the anti-resonance peak of an old AIN LWR simulations where the mesh conversion study of this thesis was done on. In the first graph the mesh size in all other dimensions had the largest possible mesh element size. While at the middle graph the bridge has the smallest mesh element size used in this study over the bridge sections. And by comparing these two we can see that the peaks do not change based on the bridge mesh. However, having a large mesh element size over the bridge section makes the device prone to generate spurious modes in the result. Considering that having a small mesh element size is necessary for an accurate band gap simulation, so using any larger element sizes then 8 cells per half wavelength is not desirable. This can also be seen in the graph below, where we can see the device resonance break down when using small mesh element sizes in the longitudinal direction. This trend was only seen when not applying the PCS array on the bridge.

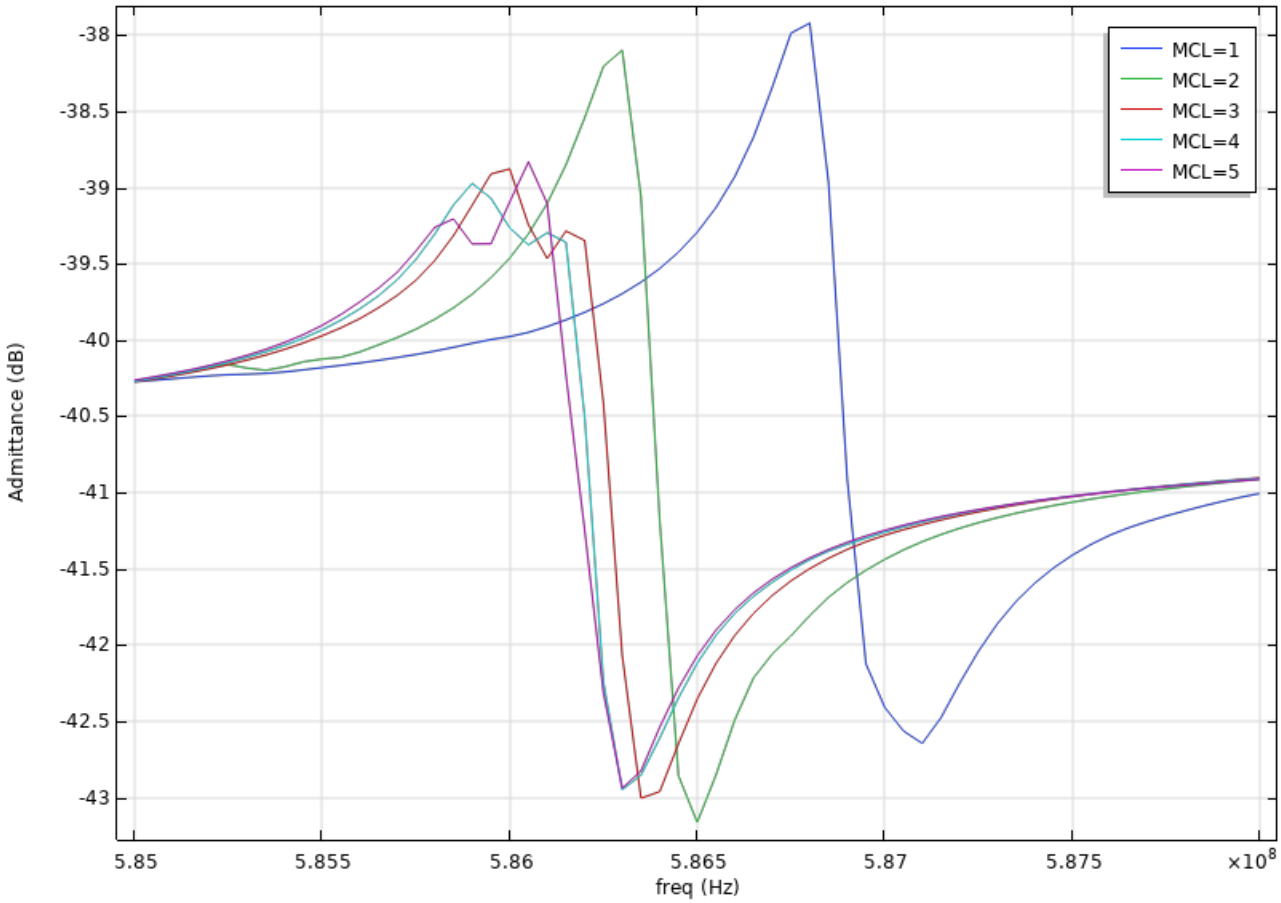

Figure 3.12 Showing an S0 mode resonance of an old AIN LWR device simulation, with changing mesh size in the longitudinal direction

The last graph above has the smallest used mesh element size used in all other direction, changing only the mesh element size in the longitudinal direction. Here we can see the anti-resonances converges to a point. Using 4 units per half wavelength gives us a result far off the rest of the results we can see in this graph. Making this mesh element size unsuitable. However, going up to 8 then 16 units per half wavelength we can see that it begins to settle down. And going from 16 to 20 units per half wavelength the relative change to the peak is severely reduces again. We can see going from 8, 16 and 20 that going from 8 to 16 units that the relative change in anti-resonance peak begins to converge with a finer mesh refinement. Considering this and the fact that using a larger unit size per wavelength to reduce the simulation time, we went with using as close to 12 units per half wavelength in the longitudinal directions for all our LWR device simulations.

Going by what we did above for the longitudinal mesh convergence, we know that we can only begin to see a relevant mesh convergence using a small unit size for the mesh in all other

directions. Where in the two figure below we can see the mesh convergence for the transverse and sweep directions respectively.

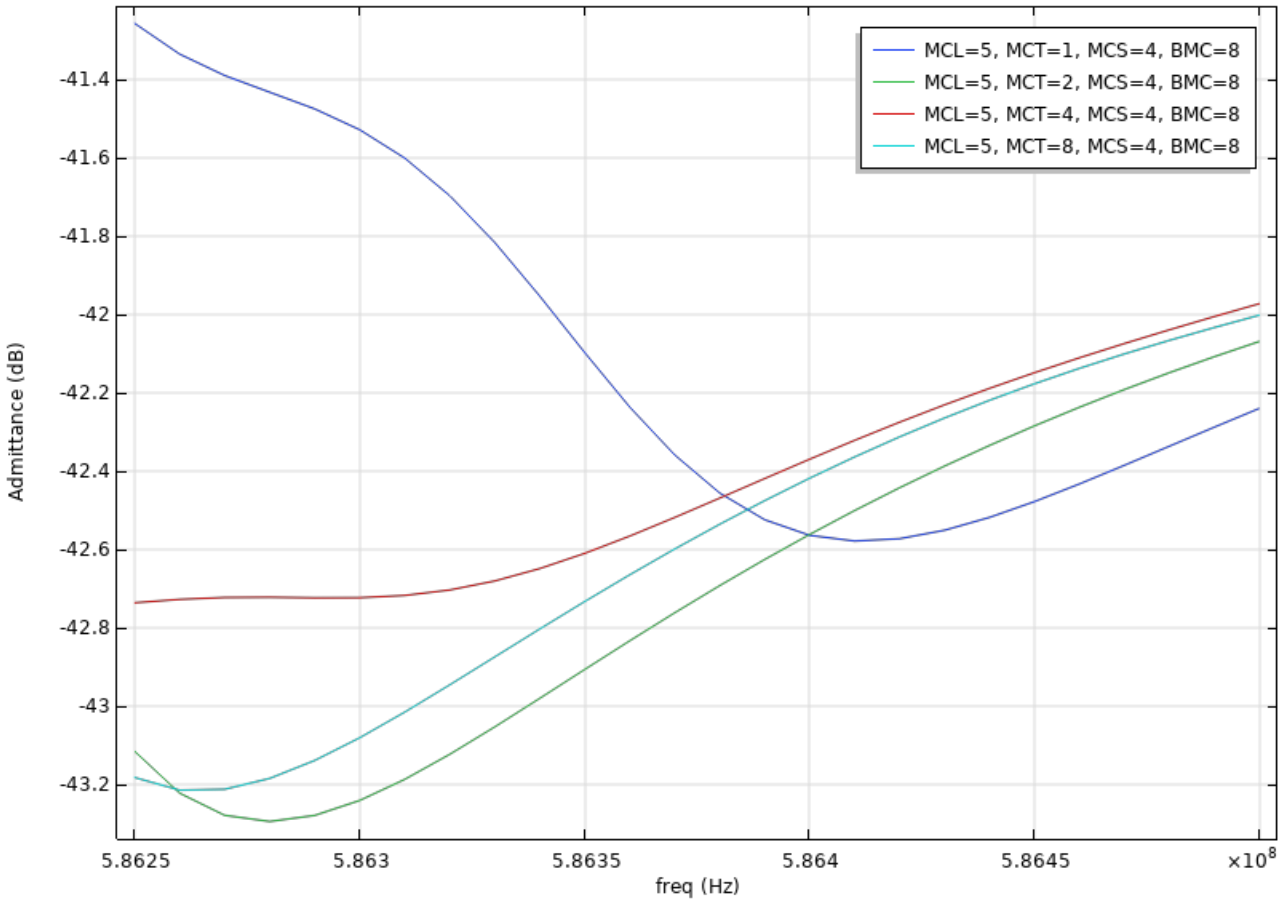

Figure 3.13 Transverse mesh convergence graph

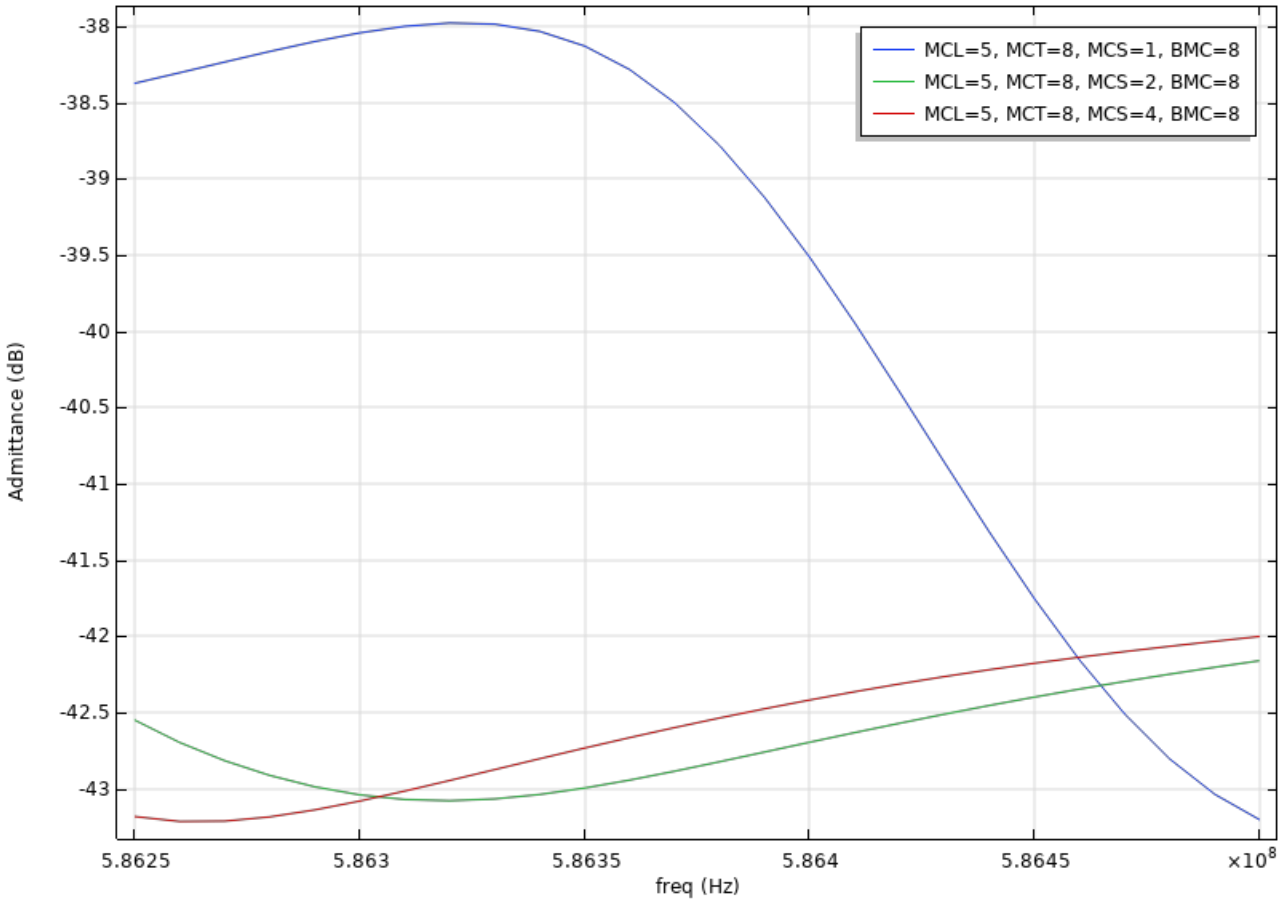

Figure 3.14 Sweep mesh convergence graph

Going by the same principle as the mesh convergence in the longitudinal direction, we can come with the conclusion that using a minimum of 5 units per half wavelength in the transverse direction and 2 units in the sweep of the device. In the figure above we can see a lot of the peaks are having spurious modes interfering with the peak. However, we can still visible see the converges of where the peak should have been and assume a minimum mesh element size. For the sweep it refers to the mesh elements per material layer in the thickness direction of the device, so a minimum of 2 units in the sweep is necessary. In the metallic layer only one sweep will be used as this layer is much thinner and is not the main medium for propagation of the waves.

3.5 Material parameters

In this project it was decided that we were going to investigate two different materials for the piezoelectric material of the LWR device. As mentioned previously these being AlN and $LiNbO_3$. As for the material properties of the materials, this were extrapolated from different sources. The

material properties of AIN are simply from the COMSOL material database and can be seen in the appendix. This stems from the fact that we are looking into the 000-plane cut of AIN. So, there is no need to change the COMSOL's database for AIN material properties, as COMSOL assumes 000 plane unless specified. However, the material properties of $LiNbO_3$ we are using are form the YX36°-cut of $LiNbO_3$. So, to get a correct material properties we need to rotate the coordinate of the 000 plane $LiNbO_3$ [25]. And as to get the correct rotations we need to investigate the Euler's angel for $LiNbO_3$. For the YX36°-cut of $LiNbO_3$ can be found by looking the table below.

Table 3.4 The corresponding Euler's angles to different crystallographic cuts of $LiNbO_3$ from [26]

Euler's angles (°)	X-cut	Y-cut	Z-cut	XY α°	XZ α°	YX α°	YZ α°	ZX α°	ZY α°
ϕ	0	0	0	0	0	0	0	0	0
θ	90	90	0	90+ α	90	α-90	90	- α	α
ψ	90	0	0	90	90- α	0	- α	0	90

So, for our cut we need to introduce a rotation a -54° rotation for the θ direction of the material. This can be done with applying this coordinate rotation to the appropriate boundary conditions in COMSOL. However, here we chose to just apply this rotation directly to the material properties and can be seen in appendix C. As for the material for the metallic layer and the slabs of the PCS structure are all simple material where the parameters were again taken from the COMSOL material database. These materials being an aluminum layer for the metallic layer. And for the slab structure we ended up using platinum for both LWR devices. As this had been proven to be the most suitable material to create a large bandgap over the desired region for a AIN LWR in other studies [18]. And this trend proved to stay consistent on the $LiNbO_3$ LWR device as well. So, no deeper look into the possibility of using a different material, for the optimization of the band gap, was deemed necessary.

4 Results

Under this segment we will talk about the results obtained using the designed FEM models. Firstly, we will check for the frequency response of the desired mode for each LWR device. Then we can investigate optimizing a PCS array for the found frequency response of the different devices. After that we will show the effective transmission rate of acoustic waves with and without the PCS array on a bridge structure. Lastly, we will go into the results of the LWR device simulations and the effective change in the admittance and quality factor of the device because of the PCS array over the bridge section of the devices.

4.1 Mode Response Range

Designing a proper band gap for the PCS is critical to be able to see any change in the device admittance response. However, even if this was the first thing to optimise for the system it must be done after finding the desired modes frequency respond. So, the first thing that was done is a simple frequency simulate sweep for each of the three different LWR devices made. We also did a cut of the devices as seen in the picture below and plotted the displacement vectors along the cut. Here we can see that in the AIN device we have an even distribution of displacement along the thickness of the devices. Something that indicates that this is most likely the S0 mode we are looking at, as this simple displacement field is only common in the S0 mode. This mode resonance was found at 608.57 MHz and anti-resonance at 608.79 MHz. However, it is very important to note that this would indicate a very low K_{eff}^2 coefficient in this device. Making this device mainly suited for a sensor device and not for a telecommunication device.

Figure 4.1 Displacement field vector of the cross section on AIN device

As for the $LiNbO_3$ device simulation we were looking for the SH0 mode not the S0 mode. So, the same principal was done on the periodic $LiNbO_3$ simulation to check the displacement field of the

found device response. However, as this is the SH0 mode we looked at the displacement along the y direction, as the tensor field would not be well suited to find the SH0 mode. In the figure below we can see the displacement along the y direction in the cross section of the $LiNbO_3$ device. This was done with the periodic device model, and here we can see a clear SH0 patter for the displacement field.

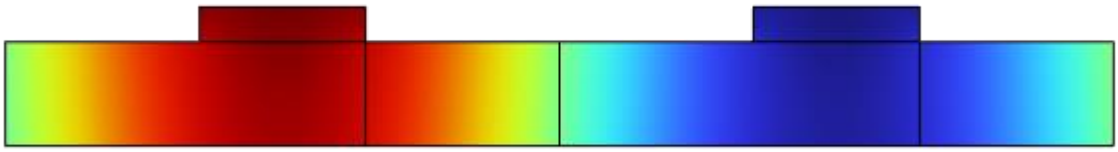

Figure 4.2 Displacement field of the cross section on $LiNbO_3$

Here the mod resonance was found at 1061 MHz, while the anti-resonance differs between the periodic and finite $LiNbO_3$ simulations. Where the anti-resonance for the periodic simulation is 1420 MHz and 1296 MHz for the finite model. It is also worth noting that the found device responses using the rough estimations found in equation 2.62 and 2.66 are only off by around 1% for the simulated device responses found here. So, even if the estimations assume an isotropic ideal plate, they are still a very accurate way to estimate the device response. And is another strong indication that these are the S0 and SH0 modes responses, for their respective devices.

4.2 PCS Band Gap

With the band gap simulation we have assumed that the honeycomb structure of the PCS array would give us the most suitable band gap in reference to the paper on "Anchor Loss Reduction of Lamb Wave Resonator by Pillar-Based Phononic Crystal" done by Yinjie Tong and Tao Han. [18] Doing so we can find an optimized band gap for the AIN PCS cell quite easily, as we could use their paper as a reference for what material to optimize our band gap with. However, as stated previously the effect of using different materials for the PCS slabs on the $LiNbO_3$ PCS cell followed a similar pattern as the AIN PCS. So, it was decided that using platinum PCS slabs would suffice for this PCS array design for $LiNbO_3$ as well.

Starting off we did a quick sweep where we checked the PCS bandgap changes with a change in the PCS slab height and radius. When changing the height of the PCS slab the bandgap tends to follow a linear curve. Where it will push the bandgap to a higher frequency with a lower slab up to where it

begins to plateau when the slab height is about 70% of the substrates thickness. This trend can be seen in both the PCS cell bandgap and the metallic layer bandgap, as seen in the figure below.

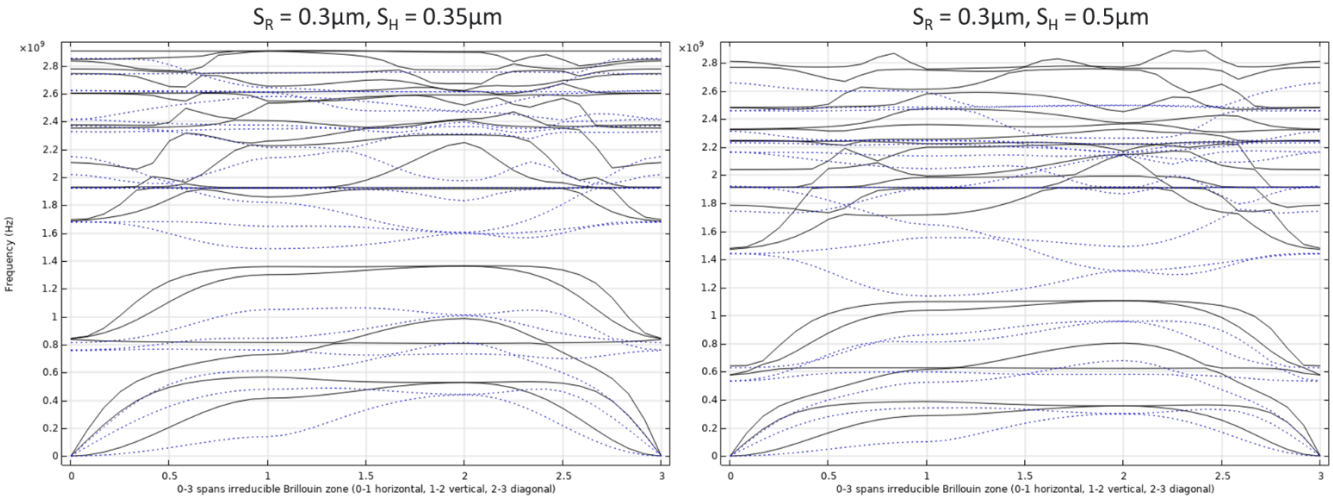

Figure 4.3 $LiNbO_3$ bandgap change with a PCS slab height change. S_R = 0.3µm, S_H = 0.35µm and 0.5µm

However, the change in PCS radius had a somewhat more unpredictable behaviour. This problem got more complicated when we noticed the importance of the metallic layer bandgap. As this bandgap got pushed vastly higher, with an increase in the PCS radius from 0.3 µm to 0.35 µm. So, designing a PCS array for $LiNbO_3$ where the design is realistic to produce and have a large enough coverage for the device resonance can prove difficult. In the figures below we can see the effect of increasing the PCS radius for the $LiNbO_3$ PCS bandgap designed for 1100MHz.

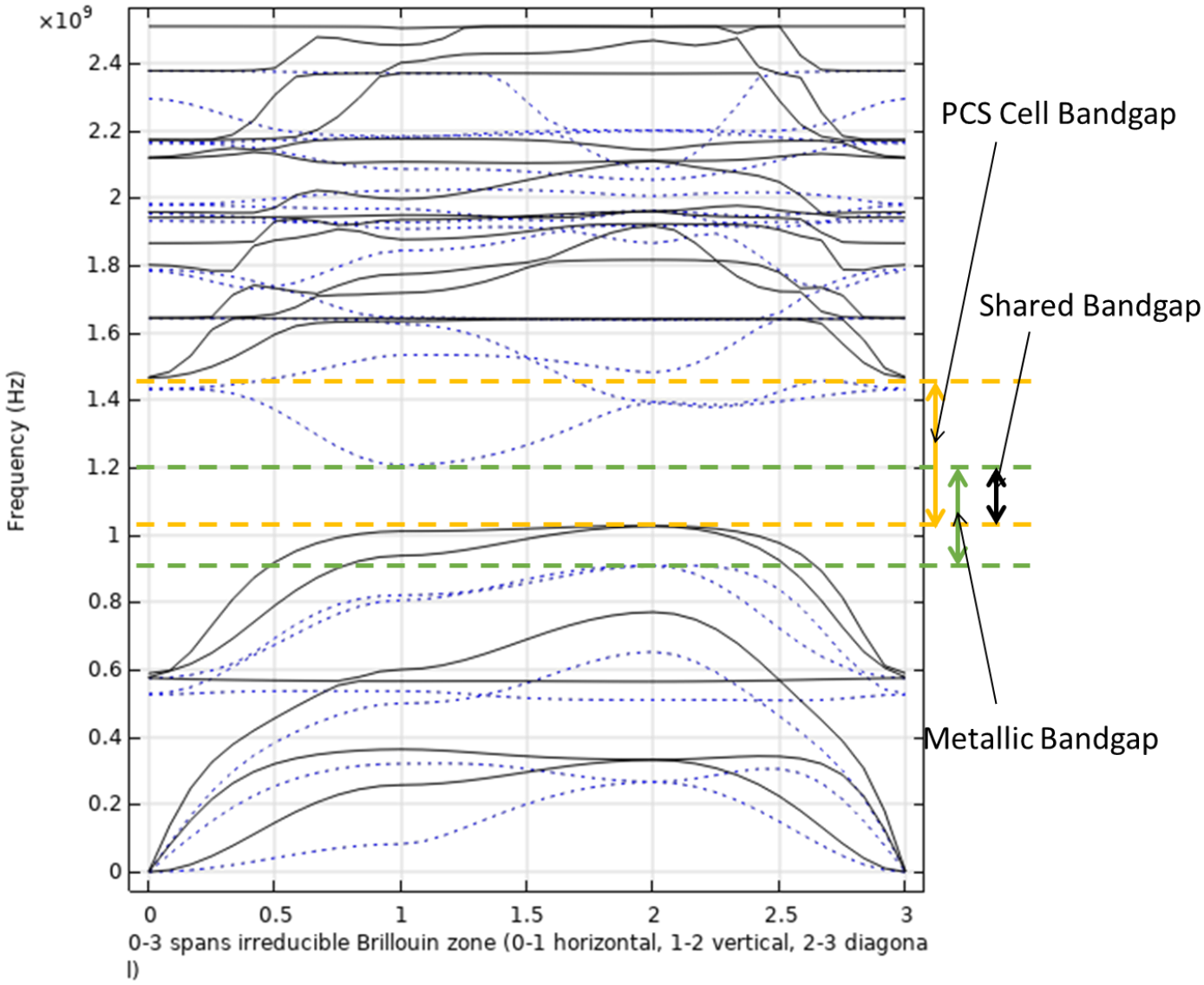

Figure 4.4 The optimized $LiNbO_3$ PCS bandgap for 1100MHz with slab radius 0.35µm, blue dotted represent the metallic layer and black lines the cell bandgap

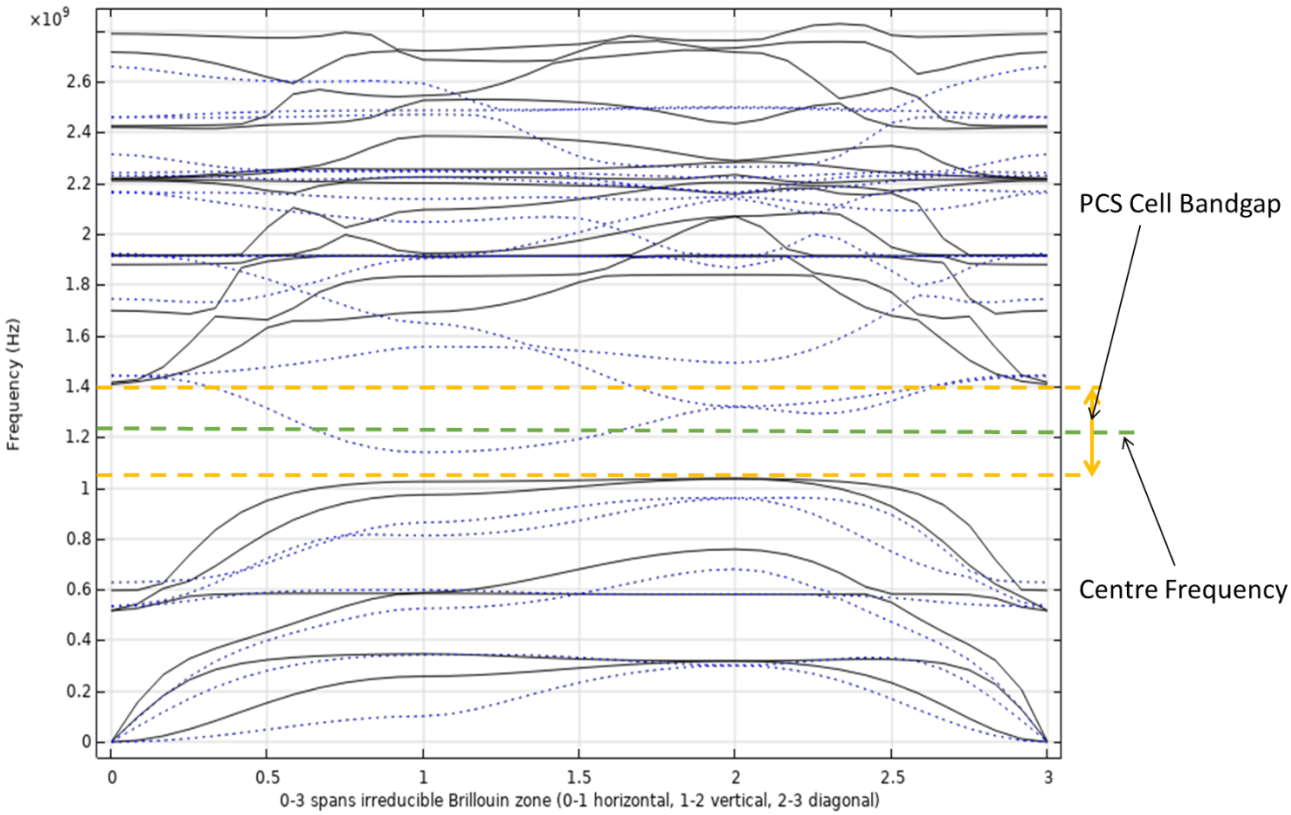

Figure 4.5 An optimized $LiNbO_3$ PCS bandgap for 1100MHz with slab radius 0.3µm, blue dotted represent the metallic layer and black lines the cell bandgap

So, for $LiNbO_3$ PCS array we ended up using a slab radius of 0.35 µm. However, we were unable to make a bandgap that could effectively entail the resonance and anti-resonance of the $LiNbO_3$ LWR device. This made it so we made the PCS array design for the following resonances peaks: 1100MHz, 1300MHz and 1400Mhz where the PCS slab height for these designs are: 0.55 µm, 0.45 µm and 0.425 µm. As stated, we could we reference a previously done paper for the AIN PCS design, where we ended up using a slab radius of 1.4 µm and a slab height of 0.8 µm. However, this bandgap did prove to be somewhat faulty later, as we noticed the effect of adding a metallic layer on the bridge section and the importance of the metallic layer bandgap. A figure of the AIN PCS bandgap can be seen below.

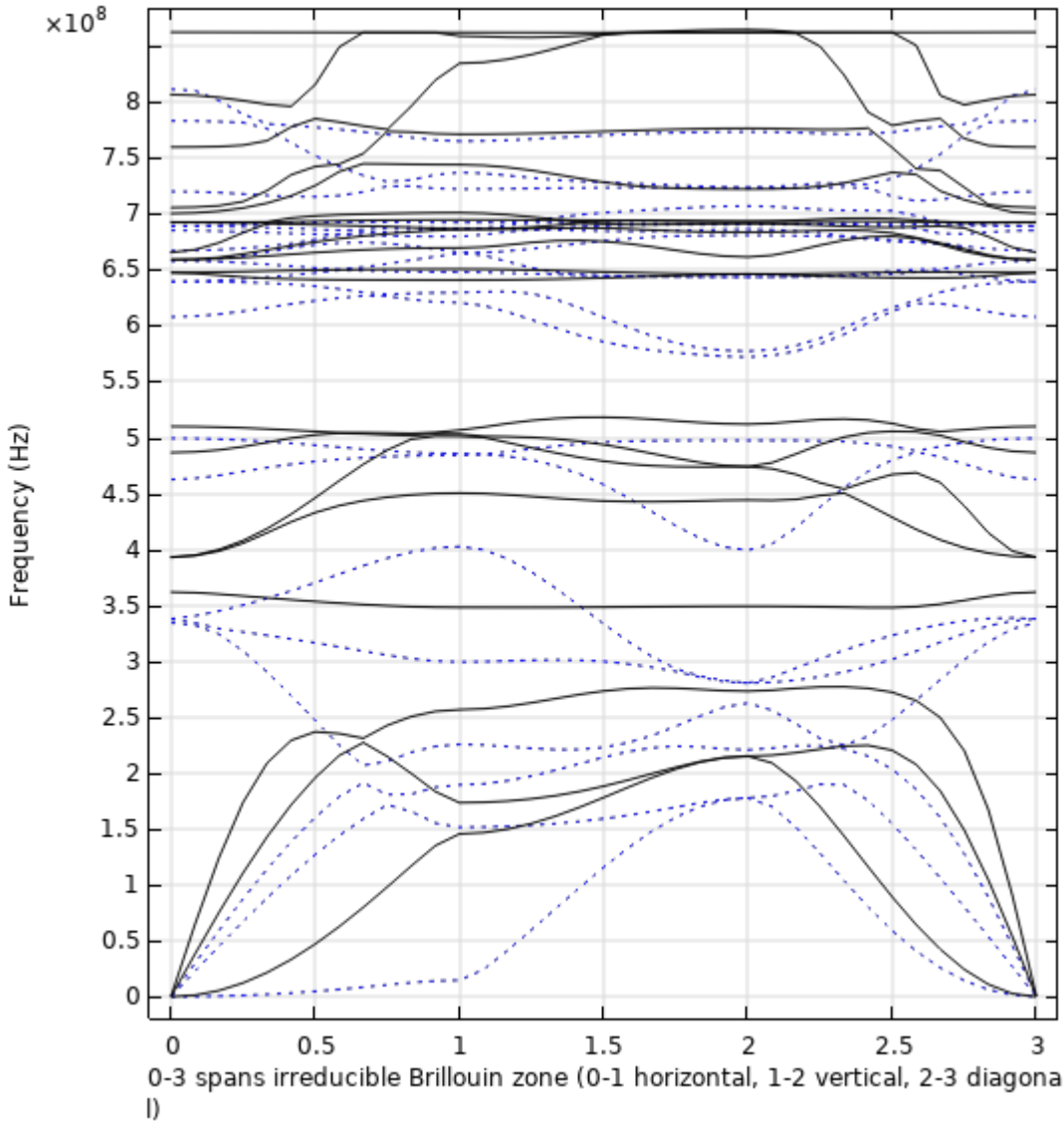

Figure 4.6 The optimized AIN PCS bandgap for 600 MHz, blue dotted represent the metallic layer and black lines the cell bandgap

4.3 Bridge transmission

Next with the knowledge of the parameters for our desired PCS geometry, we went into testing the functional suppression of acoustic wave over a bridge section. Here we looked at the relative transmission rate of a predefined displacement at one end of the structure to the other end as seen in equation (3.1). Doing so we could see a clear reduction in relative displacement from port 1 to port 2. Early on in this study the direct impact of this step was underestimated. This was because of underestimating the effect of the metallic layer over the bridge section had on the PCS array. In the

figure below we can see the relative displacement for the old AIN LWR design compared to the used PCS bandgap.

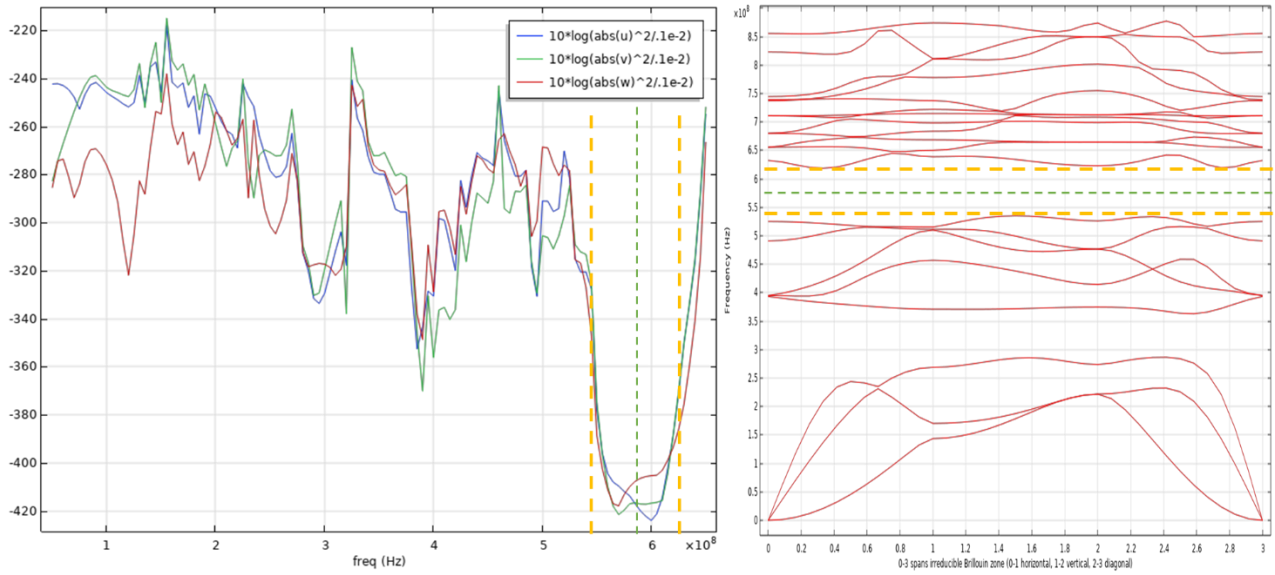

Figure 4.7 Relative displacement of an old AIN LWR design and the used PCS bandgap. u, v, and w represent x, y, and z directions respectively

Here we can see a clear relation between the ideal PCS array bandgap and the relative displacement over the bridge. So, when the new AIN LWR design was made with a similar PCS array bandgap, we assumed that the bridge simulation must have been faulty. This also comes form the fact that the new design did see an increase in the Q factor, even if the increase was smaller. In the figure below we can see the relative displacement of the new AIN LWR design compared to the used PCS bandgap.

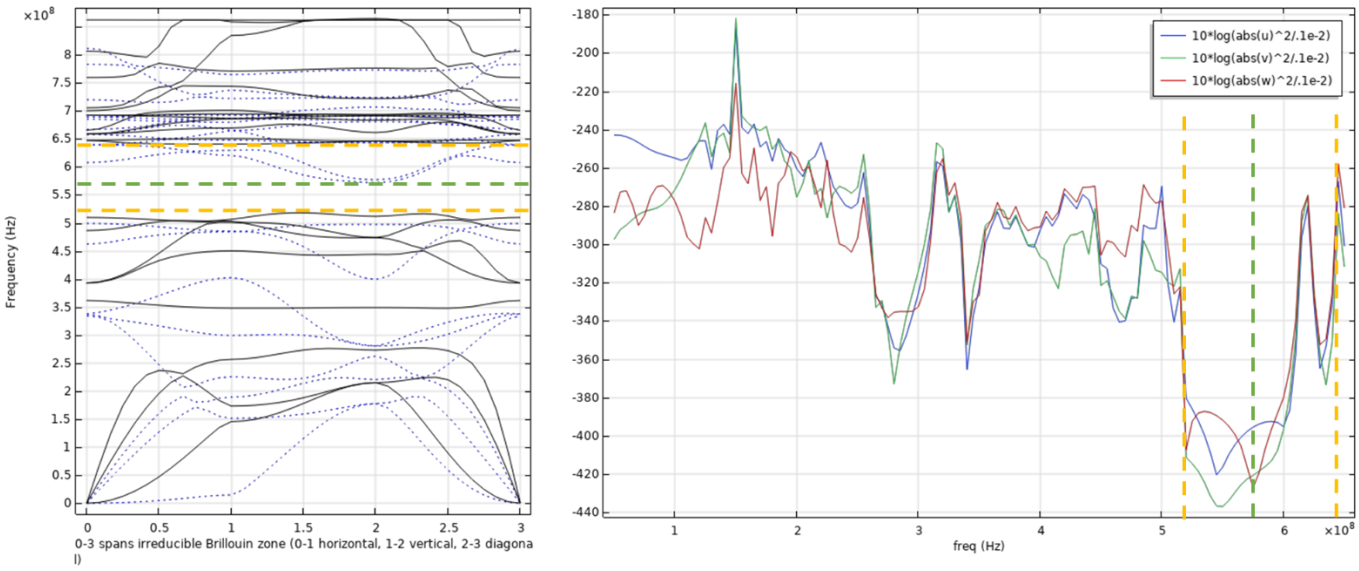

Figure 4.8 Relative displacement of the AIN LWR design and the used PCS bandgap. u, v, and w represent x, y, and z directions respectively

We can also see how this is caused by a non-infinite PCS array when looking at the displacement where the leakage happens under the bandgap. This can be seen in the figure below, where we can see a clear leakage over the sides of the bridge section. While the centre region that is relatively closer to the ideal infinite PCS array there is little to no displacement.

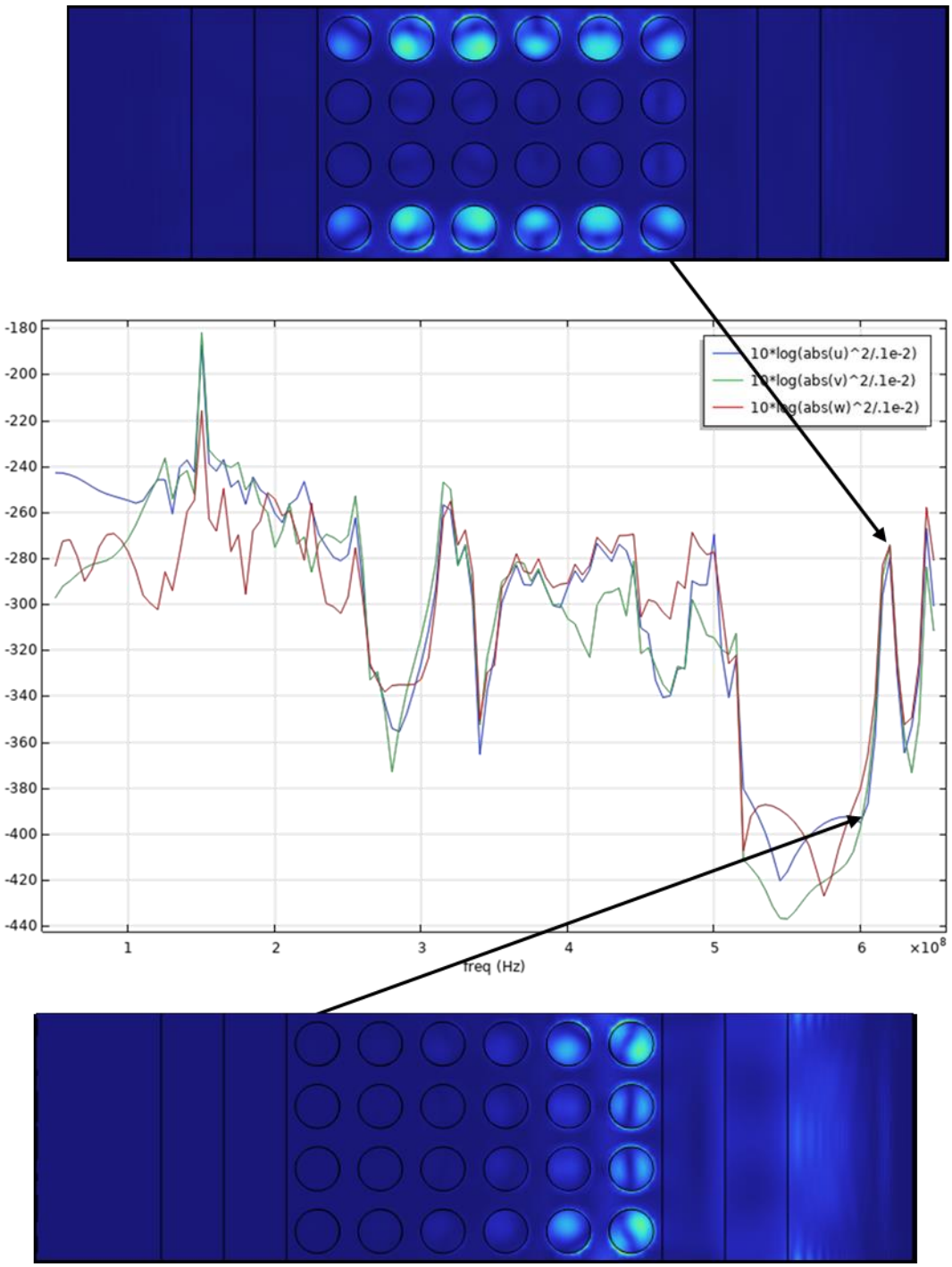

Figure 4.9 Model displacement in PCS bandgap

So, from this point forward we had to take extra precautions with designing the PCS bandgap with the metallic layer bandgap in mind. Doing so we designed the $LiNbO_3$ PCS bandgap like discussed in the above section. Below we can see the relative displacement over a $LiNbO_3$ bridge section using the PCS array designed for 1100MHz. Here we can again clearly see the strongest effect for the PCS array where the two bandgaps overlap. The same effect was seen on the PCS array designed for 1300MHz and 1400MHz.

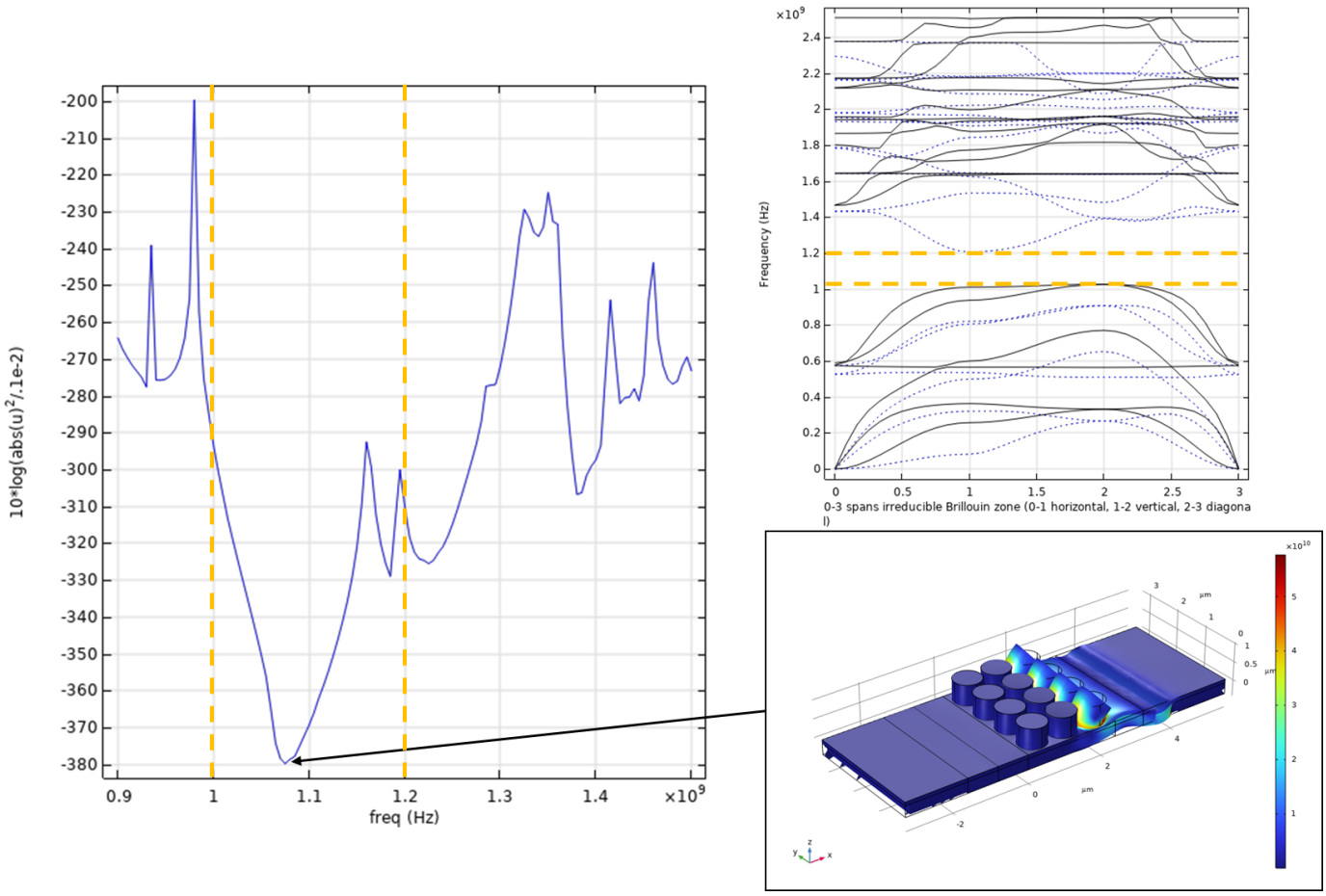

Figure 4.10 The relative transmission rate over a bridge structure with $LiNbO_3$ piezoelectric layer. u represent the x direction

4.4 Lamb Wave resonator quality factor

With the functionality of the PCS array tested for, and an optimized PCS array found for the different LWR device resonance. Now we proceeded to test the implementation of these PCS array onto the bridge section of the different LWR devices, to see the effect they would have on the Quality factor of the device. To start we had investigated the impact of the PCS array on the AIN LWR device. This where we first noticed the importance of the metallic layer in the PCS array. As stated earlier in the beginning of the study we used a different AIN LWR design, were we abstained from using a metallic layer on the bridge and outer section on the device to limit the variables that could affect the PCS array. Here we saw a drastic increase of 84% in the resonance Quality factor and an increase of 39% in the anti-resonance of the device. Below we can see the admittance graph

of this device, were the graph and Quality factor were made and found using the MATLAB code given in appendix b.

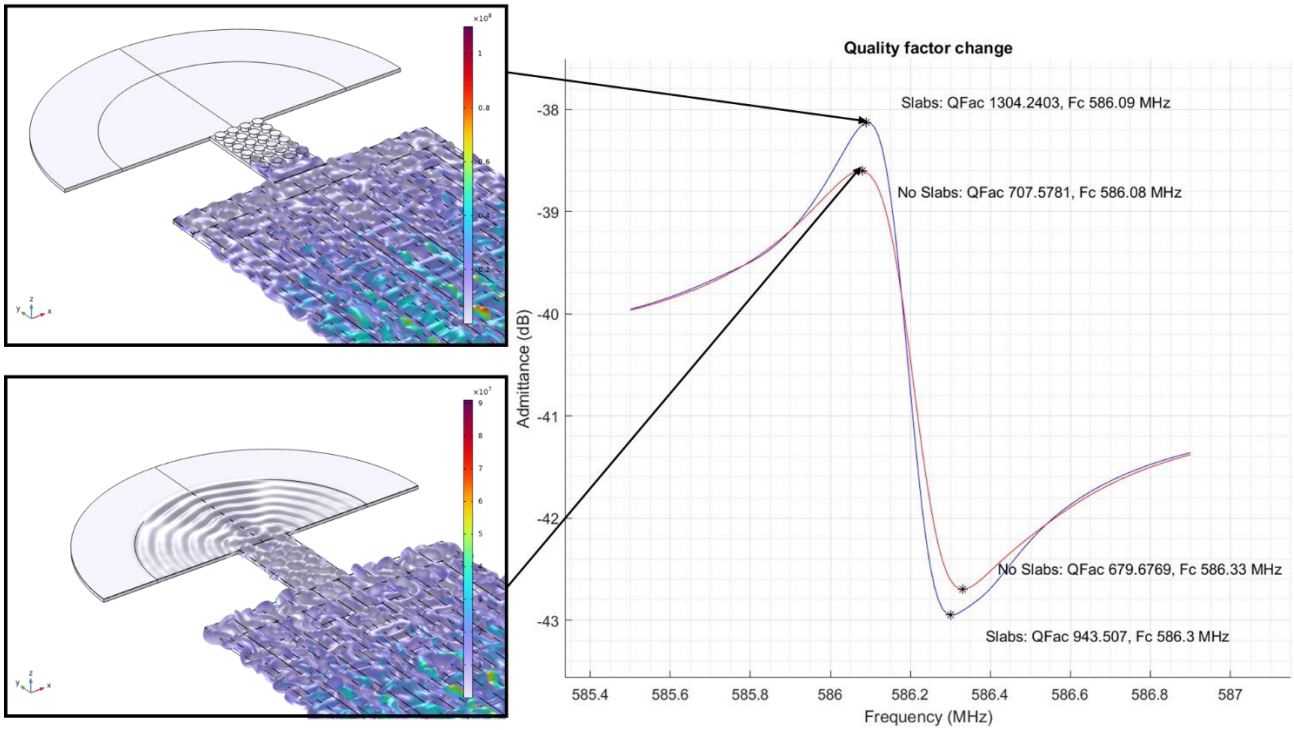

Figure 4.11 Admittance curve of old AIN LWR design

Here we can see the Quality factor increase from 707.57 to 1304.24 on the resonance of this device. While having a slightly weaker increase going from 679.67 to 943.5 on the anti-resonance. Now when we compare this to the newest AIN LWR design where the outer section was covered with a metallic layer, and we used aluminium for the metallic layer in contrast to platinum we used on this design. Here in the figure below we can see an over that the new device has an overall higher Quality factor on the device. However, we get a lesser increase in the device Quality factor by adding the PCS array on the bridge.

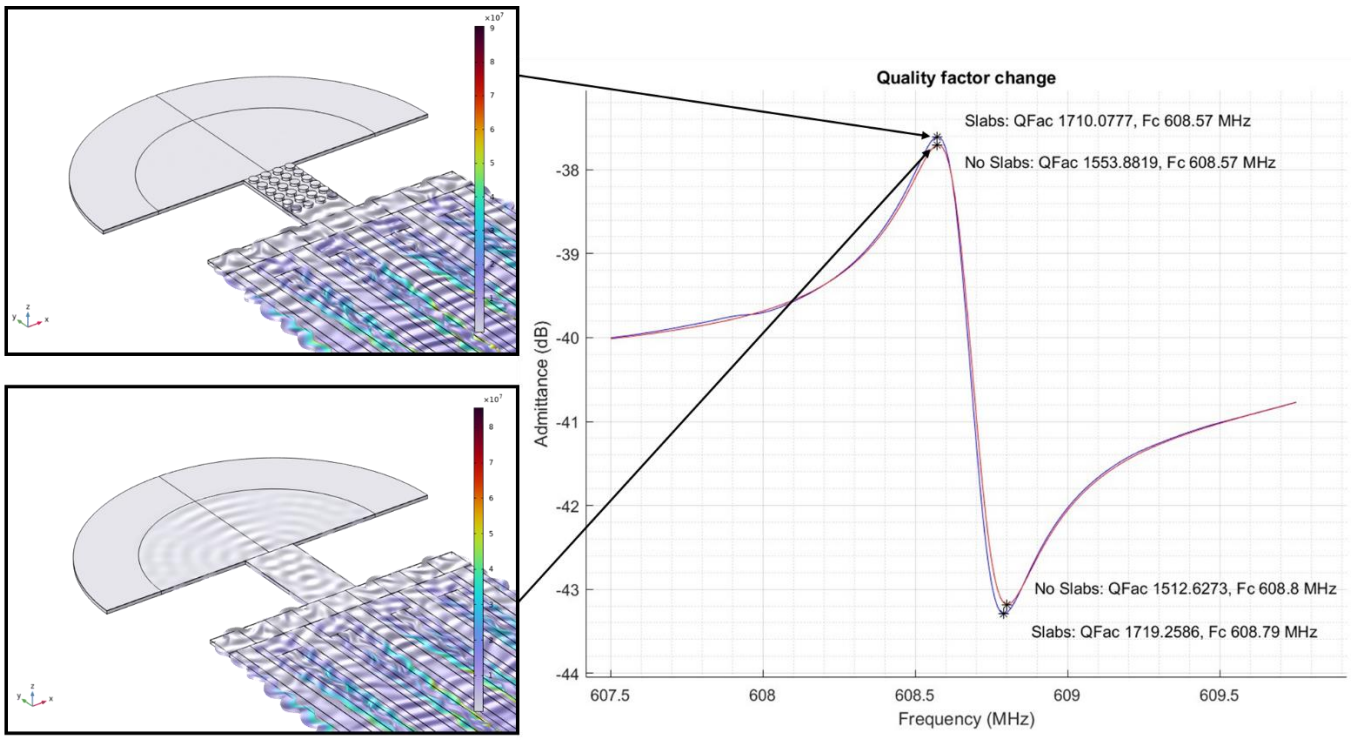

Figure 4.12 Admittance curve of current design AIN LWR design

Here we see the Quality factor of the resonance increase from 1553.18 to 1710.07 and in the anti-resonance we see an increase from 1512.08 to 1719.25. We are still seeing some increase in the Quality factor. This comes from the fact that even if we are seeing a reduction in the PCS array ability to reduce the acoustic wave leakage because of the addition of the metallic layer. The PCS array still holds some ability to reduce the displacement propagation at this frequency, as this PCS design does not break down completely before 620MHz.

Now going over to the $LiNbO_3$ LWR devices we understood the importance of designing the PCS array with the metallic layer in mind. So, first we designed a PCS array for the periodic $LiNbO_3$ simulation. However, because the interference of the metallic layer we could not design a PCS array that could cover both peaks of the SH0 resonance. To mitigate this, we designed 2 different PCS array, one for the 1100Mhz region and one for 1400MHz region. But as the 1100MHz PCS array was designed to cover both peaks in an ideal infinite array, we can see the effect on both peaks in this array. This stems from the fact that as this is an infinite periodic simulation, we are not seeing the interference of the metallic layer as we see in a non-infinite array. In the figure below we can see three different simulations, here we can see a periodic simulation with and without the PCS array. But there is also a third simulation data where we had an etched edge to simulate what an ideal device response would be with no leakage of energy over the bridge.

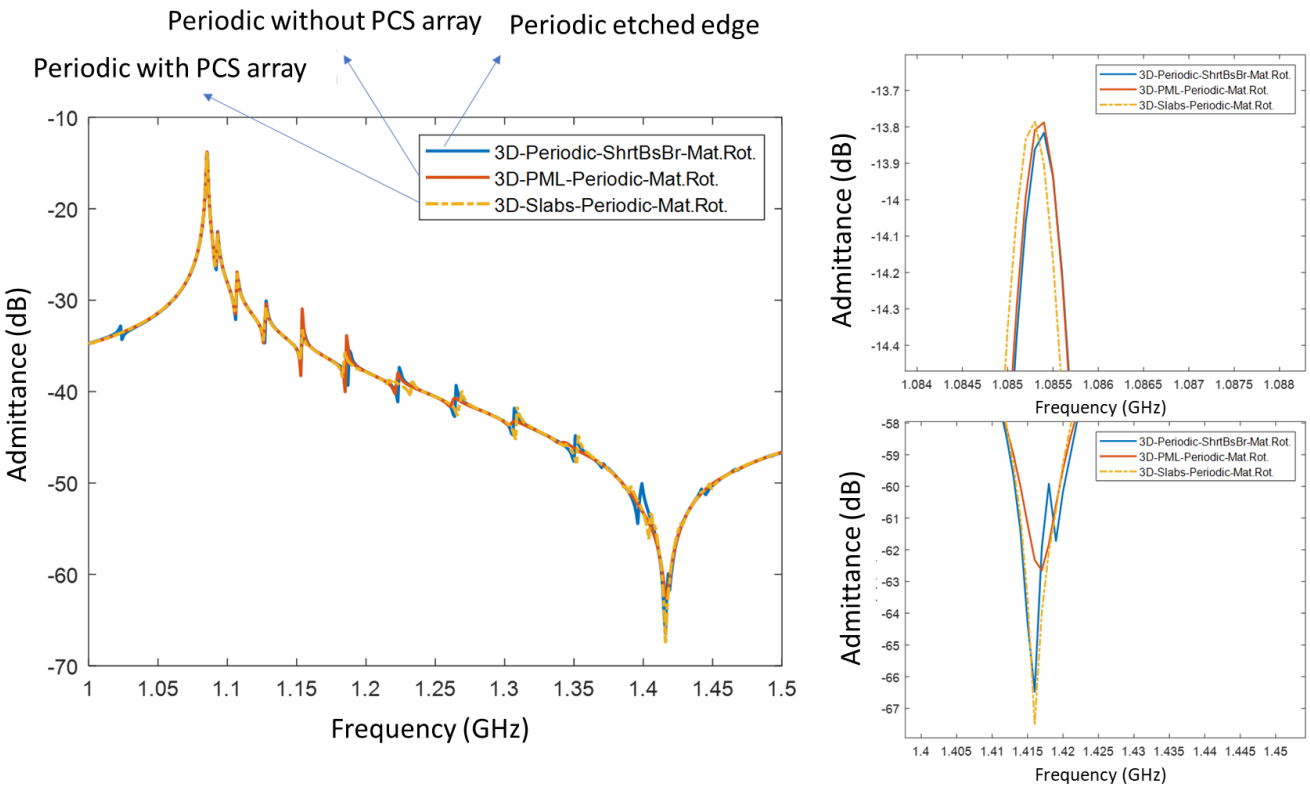

Figure 4.13 Periodic $LiNbO_3$ LWR design admittance response

In this result we noticed something interesting, this being that for the SH0 mode using our simulation boundaries we do not see any energy leakage over the bridge section on the resonance peak. We can see that this must be the case as we see a near identical resonance peak for all three simulation designs. However, at the anti-resonance we can see a drastic change in the peak with the use of a PCS array. As the anti-resonance peak of the simulation using the PCS array have a result very close to the etched simulation results, indicating that the PCS array have managed to stop most of the leakage over the bridge section in this simulation. So, when doing the finite $LiNbO_3$ LWR simulation we used the PCS array designed for the anti-resonance around 1300MHz as we most likely won't be seeing any leakage of energy over the resonance. In the figure below we can see the simulation result of the SH0 mode using the finite $LiNbO_3$ LWR simulation. Here we can see that the resonance peak has no change with or without the PCS array as assumed. However, we can see a large increase in the Quality factor of the anti-resonance peak of 195% going from a Quality factor of 158.58 to 468.18 with the use of the PCS array over the bridge section.

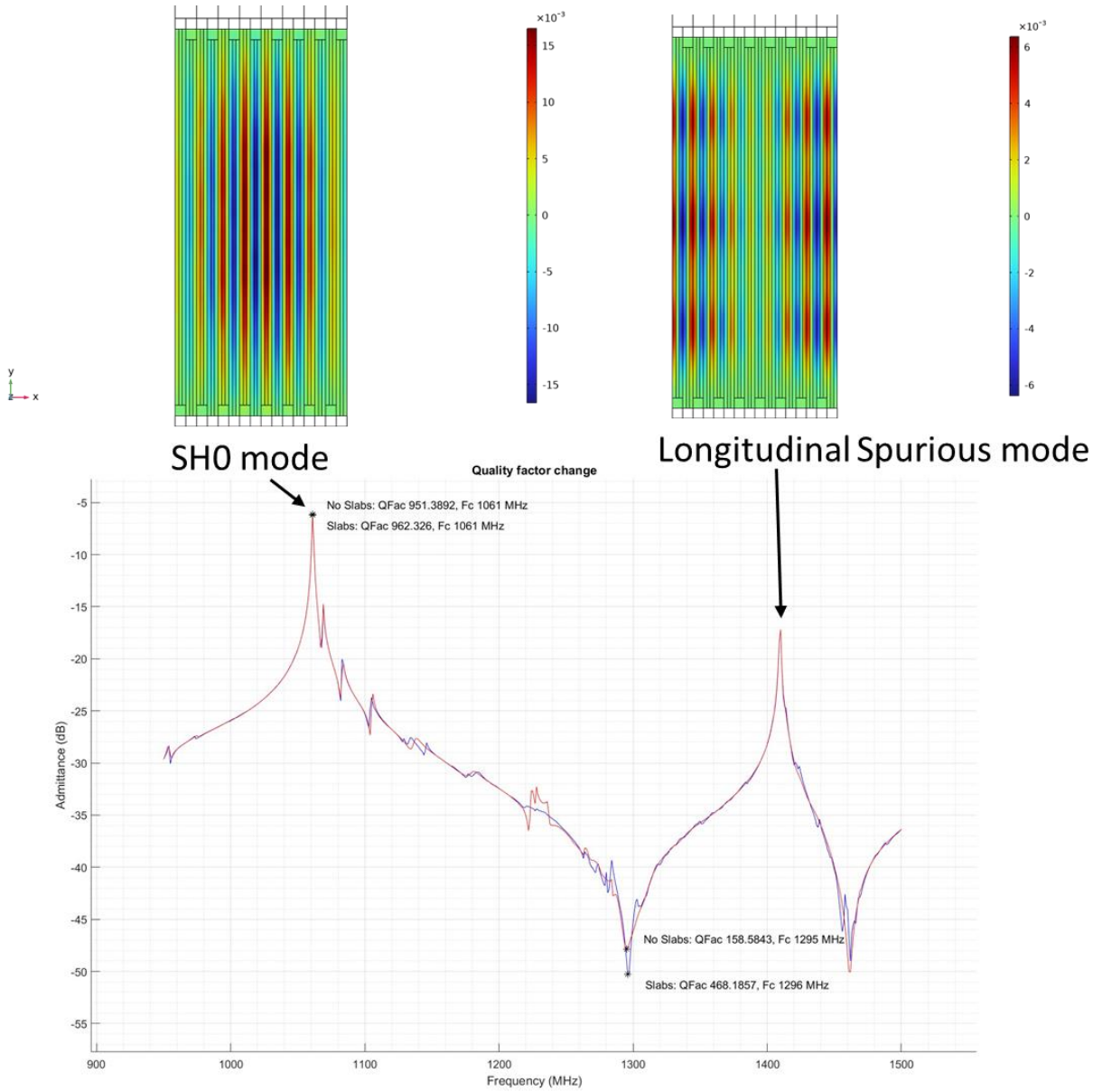

Figure 4.14 Admittance curve for finite $LiNbO_3$ LWR simulations

In this mode we can see some spurious modes within the device response we are looking at. In the paper of Silvan Stettler and Luis Guillermo Villanueva, they suggest that these are spurious SH modes, and the possibility of reduce the impact with a change to the substrates geometry [5]. However, most of the changes that have any significant impact on the reduction of these spurious modes, comes with the price of a reduced anti-resonance Quality factor. So, there might a possibility of using a PCS array to mitigate these changes. As the PCS array have a very minimal impact on the overall appearance of these spurious modes but introduces a large increase in the Quality factor of the device.

5 Discussion

5.1 Possible design flaw and limitations

Over this study we have gone over the design procedure for designing a functional PCS array for a given LWR design. However, it is worth noting that this all assume a theoretical perfect material parameter. So, even if there has been some design consideration for the fabrication of said design, there is still a very accurate and difficult fabrication needed to be able to see a similar result on a real device. Some of the problem comes from different design parameters, one of which is the sensitivity of the PCS slab on the PCS array bandgap. When looking at the PCS array designed with a bandgap around 1100MHz for a $LiNbO_3$ device, we can see a large shift in the metallic layer bandgap going from 0.3 µm to 0.35 µm. So, any error in the fabrication result compared with the ideal design can be the difference between a functional and non-functional fabricated device. Where there is also worth noting that creating a slab design with a radius of 0.35 µm allows only a room of 0.1 µm in-between the slabs.

We can also see a clear limitation in the possible PCS bandgap one could design. Where we would ideally design a PCS bandgap with a centre frequency as close to the resonance peaks as possible. When designing a PCS design for the S0 AIN LWR device this would be a concern as the peaks are essentially at the same frequency. In contrast then the SH0 $LiNbO_3$ LWR we have a large gap between the two peaks, so in this scenario it becomes very difficult to design an ideal PCS bandgap for this device. This also becomes impossible with our simple PCS design when considering the interference form the metallic layer in the non-infinite PCS array. One potential fix could be to scale the PCS array, as we can see this effect even when only using an array of 3 PCS. So, there is a potential to add different PCS design after the last on one the bridge structure, so one could potentially use 2 or 3 PCS slabs of one PCS design before changing the slab parameters to a different design made for a different frequency.

It is also important to note that every simulation in this study assumes perfect material structure and minimal outside interference on every simulation done. Where all the device loss comes from the isotropic loss factor added to the material, or the PML absorption on the outer region of the bridge and LWR simulations.

Lastly noting that we got a very small K_{eff}^2 on the AIN LWR device, this can be because of using AIN for the substrate. It can however be because of having a very high loss factor with a relatively small capacitance between the IDT fingers and few IDT in total for the device. Where the $LINBO_3$ device a

continuous model or a finite model with 8 set of IDT compared, to the Ain device running only 4.5 set IDT. Where the $LINBO_3$ device also boast a 4 times higher capacitance between the IDT fingers compared to the AIN device.

5.2 Future aspects

As seen under this study we have seen a clear increase in the quality factor the LWR devices when an optimized PCS array could be design for a specific frequency range of an LWR devices. This gives a clear image of the possibility of an improved LWR device though the reduction in energy leakage over a bridge section on a device, without the need to reduce the structural integrity of the device with a smaller or less stable bridge design. So, the possibility of a more functional LWR device is becoming more and more feasible by the year, as more realistic LWR device design and optimizations are being work on and made possible. It is also worth noting that the PCS array not only have a great potential to stop the transmission of acoustic waves under the designed band gap, but that the edges of PCS array also show a potential to create an accumulation of displacement in a designated area. Were this might be used to emphasis certain modes of the device to make the device have a stronger response for this mode. This however is just a speculation and for functionality of using this accumulation of displacement energy for anything is still just a vague idea. However as shown in this study, the PCS array does show a strong ability to create an increase in the quality factor of a LWR device with the use of an optimized PCS array. The problem is that this does implies the possibility of being able to create an optimized PCS array. The problem here is that there is a strong limitation in how much the centre frequency and band gap can be changed with merely simple geometrical or material changes in a simple PCS design. So, there is a lot of potential in looking into further optimization of the PCS array with the use of more complex slab structures. As there might be other PCS design that could mitigate the interference of the metallic layer. Allowing us to see a PCS array with a functionality closer to the ideal PCS bandgap.

6 Conclusion

With everything shown so far, the possibility of using an optimized PCS array to stop the device leakage over the bridge section is undeniable. Where a large quality factor increase was shown possible for both the resonance and anti-resonance for an AIN LWR device. While a Large increase in the quality factor of the anti-resonance on a $LiNbO_3$ LWR device was also shown. Whereas the main reason no increase in the quality factor of the resonance was shown lied in the lack of energy loss over the bridge for the SH0 mode resonance of the $LiNbO_3$ device. So, the application of applying a PCS array to stop device energy leakage seems very promising. Where the main hurdle would be to fabricate an appropriate PCS array on a physical device. AS the bandgap of the PCS array is very sensitive to changes in the PCS cell parameters.

Bibliography

[1] S. F. RONALDS, *FATHER OF THE ELECTRIC TELEGRAPH*. ICP, 2016.

[2] S. Technology, “Telecommunication Market is Changing with Growing Integration of 5G, Big Data, and Cloud Computing,” 2022.

[3] A. Pärssinen, M. Leinonen, M. Berg, P. Kyösti, and M. Matinmikko-Blue, *White paper on RF enabling 6G : opportunities and challenges from technology to spectrum*. Oulun yliopisto, 2021.

[4] T. Baron *et al.*, “Wideband Lithium Niobate FBAR Filters,” *Int. J. Microw. Sci. Technol.*, vol. 2013, pp. 1–6, Feb. 2013, doi: 10.1155/2013/459767.

[5] S. Stettler and L. G. Villanueva, “Transversal Spurious Mode Suppression in Ultra-Large-Coupling SH0 Acoustic Resonators on YX36◦ -Cut Lithium Niobate,” *J. MICROELECTROMECHANICAL Syst.*, p. 11, 2023.

[6] Dr. Rüdiger Paschotta, “Phononic crystals,” *RP Pholonics Encycl.*, p. 1, 2022.

[7] G. Tobolka, *Mixed matrix representation of saw transducers*. IEEE transactions, 1979.

[8] N. Gupta and K. Kandpal, “Material Selection Techniques in Materials for Electronics,” 2020, pp. 1–15.

[9] M. Yogendrappa, “PCB Material Selection: Electrical and Manufacturing Considerations,” *Sierra Circuits*, 2021.

[10] J. Zou, “High-Performance Aluminum Nitride Lamb Wave Resonators for RF Front-End Technology,” UC Berkeley, 2015.

[11] SPTS Technologies, “AlN PVD for RF & MEMS,” 2019.

[12] Y. Yang *et al.*, “Solidly Mounted Resonators with Ultra-High Operating Frequencies Based on 3R-MoS 2 Atomic Flakes,” *Adv. Funct. Mater.*, Apr. 2023, doi: 10.1002/adfm.202300104.

[13] R. Web, “Demand for Fast Data Transfers Strengthens the Monolithic Microwave IC (MMIC) Market with a CAGR of 9.8% through 2032, Says Fact.MR,” *Padovanews*, p. 1, 2022.

[14] D. P. Morgan, “A HISTORY OF SURFACE ACOUSTIC WAVE DEVICES,” *Int. J. High Speed Electron. Syst.*, vol. 10, no. 03, pp. 553–602, Sep. 2000, doi: 10.1142/S0129156400000593.

[15] M. Kadota and T. Ogami, “High frequency lamb wave resonator using LiNbO<inf>3</inf> crystal thin plate and application to tunable filter,” in *2010 IEEE International Ultrasonics Symposium*, 2010, pp. 962–965, doi: 10.1109/ULTSYM.2010.5935493.

[16] Y. Xie *et al.*, “Design and Analysis of Lithium–Niobate-Based Laterally Excited Bulk Acoustic

Wave Resonator with Pentagon Spiral Electrodes," *Micromachines*, vol. 14, no. 3, p. 552, Feb. 2023, doi: 10.3390/mi14030552.

[17] J. Zou, "High Quality Factor Lamb Wave Resonators," Berkeley, 2015.

[18] Y. Tong and T. Han, "Anchor Loss Reduction of Lamb Wave Resonator by Pillar-Based Phononic Crystal," *Micromachines*, vol. 12, no. 1, p. 62, Jan. 2021, doi: 10.3390/mi12010062.

[19] P. Marty Noël, "general wave equation for elastic waves in a non-piezoelectric solid," University of London, 2002.

[20] V. Tollefsen, "AlN on Sapphire," University of South-Eastern Norway, 2020.

[21] "Euler angles," *Wikipedia*. Wikipedia, 2023.

[22] E. D. Daniel Royer, *Elastic Waves in Solid 1*. Masson, Paris: SPringer Berlin, Heidelberg, 2000.

[23] O. Schnitzer and R. V. Craster, "Bloch Waves in an Arbitrary Two-Dimensional Lattice of Subwavelength Dirichlet Scatterers," *SIAM J. Appl. Math.*, vol. 77, no. 6, pp. 2119–2135, Jan. 2017, doi: 10.1137/16M107222X.

[24] Ajay Harish, "What is Convergence in Finite Element Analysis?," *Simscale*, 2022. [Online]. Available: https://www.simscale.com/blog/convergence-finite-element-analysis/.

[25] J. Ransley, "Piezoelectric Materials: Applying the Standards," *COMSOL Blog*, 2016. [Online]. Available: https://www.comsol.com/blogs/piezoelectric-materials-applying-the-standards/.

[26] M. S. Namnabat, M. Moghimi Zand, and E. Houshfar, "3D numerical simulation of acoustophoretic motion induced by boundary-driven acoustic streaming in standing surface acoustic wave microfluidics," *Sci. Rep.*, vol. 11, no. 1, p. 13326, Jun. 2021, doi: 10.1038/s41598-021-90825-z.

Appendix A

Piezoelectric constitutive equations, symbols, and units

Table 6.1 Piezoelectric constitutive equations

$\boldsymbol{T_{ij} = c^{E}_{ijkl} S_{kl} - e_{kij} E_k}$	(A.1)
$\boldsymbol{D_i = e_{ikl} S_{kl} + \varepsilon^{S}_{ij} E_k}$	(A.2)
$\boldsymbol{S_{ij} = s^{E}_{ijkl} T_{kl} + d_{kij} E_k}$	(A.3)
$\boldsymbol{D_i = d_{ikl} T_{kl} + \varepsilon^{T}_{ik} E_k}$	(A.4)
$\boldsymbol{S_{ij} = s^{D}_{ijkl} T_{kl} + g_{kij} D_k}$	(A.5)
$\boldsymbol{E_i = -g_{ikl} T_{kl} + \beta^{T}_{ik} D_k}$	(A.6)
$\boldsymbol{T_{ij} = c^{D}_{ijkl} S_{kl} - h_{kij} D_k}$	(A.7)
$\boldsymbol{E_i = -h_{ikl} S_{kl} + \beta^{S}_{ik} D_k}$	(A.8)

Table 6.2 Symbol and units of material constants

c_{ijkl}	Elastic stiffness	$\left[\frac{N}{m^2}\right]$
s_{ijkl}	Elastic compliance	$\left[\frac{m^2}{N}\right]$
e_{ikl}	Piezoelectric	$\left[\frac{Vm}{N}\right]$ or $\left[\frac{C}{m^2}\right]$
g_{ikl}	Piezoelectric	$\left[\frac{N}{Vm}\right]$ or $\left[\frac{m^2}{C}\right]$
d_{ikl}	Piezoelectric	$\left[\frac{m}{V}\right]$ or $\left[\frac{C}{N}\right]$
h_{ikl}	Piezoelectric	$\left[\frac{V}{m}\right]$ or $\left[\frac{N}{C}\right]$
ε_{ij}	(dielectric) Permittivity	$\left[\frac{F}{m}\right]$
β_{ik}	Impermittivity	$\left[\frac{m}{F}\right]$
S_{kl}	Strain	
T_{ij}	Stress	$\left[\frac{N}{m^2}\right]$

D_i	Electric displacement	$\left[\frac{C}{m^2}\right]$
E_k	Electric field	$\left[\frac{V}{m}\right]$
ρ	Density	$\left[\frac{kg}{m^3}\right]$

Appendix B

MATLAB code used to find the quality factor of the frequency response of the different devices.

```
clc
clear all
%NOTE: W(1:350,2) is to limit the range to avoid the next resonance,
%also change mm1(+-1) if the value is at edge of data sample
%Load Simulation data Slabs
w=load('3D-Full-1300MHz.txt');
%calc anti resonance Qfac
[minn,mm]=min(w(1:350,2))
wcut=minn*sqrt(2)
w0=w(mm,1)
[mm1 nn1]=find(w(1:350,2)<wcut);
slp=(w(min(mm1),2)-w(min(mm1-1),2))/(w(min(mm1-1),1)-w(min(mm1),1));
w1=(wcut-w(min(mm1-1),2))/slp+w(min(mm1-1),1)
slp=(w(max(mm1+1),2)-w(max(mm1),2))/(w(max(mm1+1),1)-w(max(mm1),1));
w2=(wcut-w(max(mm1+1),2))/slp+w(max(mm1+1),1)
%Hold for plot
QFacSA = w0/(w2-w1)
QFacTextSA = string(QFacSA)
PeakSAFreq = w(mm,1)/1000000
FreqStringSA = string(PeakSAFreq)
PeakSAValue = 10*log10(minn)
addmitanceS =10*log10(w(:,2))
freqS = w(:,1)/1000000
%Calc Resonance Qfac
[maxx,mm]=max(w(1:350,2))
wcut=maxx/sqrt(2)
w0=w(mm,1)
[mm1 nn1]=find(w(:,2)>wcut);
slp=(w(min(mm1),2)-w(min(mm1-1),2))/(w(min(mm1),1)-w(min(mm1-1),1));
w1=(wcut-w(min(mm1-1),2))/slp+w(min(mm1-1),1)
slp=(w(max(mm1+1),2)-w(max(mm1),2))/(w(max(mm1+1),1)-w(max(mm1),1));
w2=(wcut-w(max(mm1+1),2))/slp+w(max(mm1+1),1)
%Hold for plot
QFacSR = w0/(w2-w1)
QFacTextSR = string(QFacSR)
PeakSRFreq = w(mm,1)/1000000
FreqStringSR = string(PeakSRFreq)
PeakSRValue = 10*log10(maxx)
%Load Simulation data no Slabs
w=load('3D-Full-WO Slab.txt');
%calc anti resonance Qfac
[minn,mm]=min(w(1:350,2))
wcut=minn*sqrt(2)
w0=w(mm,1)
[mm1 nn1]=find(w(1:350,2)<wcut);
```

```
slp=(w(min(mm1),2)-w(min(mm1-1),2))/(w(min(mm1-1),1)-w(min(mm1),1));
w1=(wcut-w(min(mm1-1),2))/slp+w(min(mm1-1),1)
slp=(w(max(mm1+1),2)-w(max(mm1),2))/(w(max(mm1+1),1)-w(max(mm1),1));
w2=(wcut-w(max(mm1+1),2))/slp+w(max(mm1+1),1)
%Hold for plot
QFacNA = w0/(w2-w1)
QFacTextNA = string(QFacNA)
PeakNAFreq = w(mm,1)/1000000
FreqStringNA = string(PeakNAFreq)
PeakNAValue = 10*log10(minn)
addmitanceN =10*log10(w(:,2))
freqN = w(:,1)/1000000
%Calc Resonance Qfac
[maxx,mm]=max(w(1:350,2))
wcut=maxx/sqrt(2)
w0=w(mm,1)
[mm1 nn1]=find(w(:,2)>wcut);
slp=(w(min(mm1),2)-w(min(mm1-1),2))/(w(min(mm1),1)-w(min(mm1-1),1));
w1=(wcut-w(min(mm1-1),2))/slp+w(min(mm1-1),1)
slp=(w(max(mm1+1),2)-w(max(mm1),2))/(w(max(mm1+1),1)-w(max(mm1),1));
w2=(wcut-w(max(mm1+1),2))/slp+w(max(mm1+1),1)
%Hold for plot
QFacNR = w0/(w2-w1)
QFacTextNR = string(QFacNR)
PeakNRFreq = w(mm,1)/1000000
FreqStringNR = string(PeakNRFreq)
PeakNRValue = 10*log10(maxx)
%Plot Data
hold on
grid on
grid minor
title('Quality factor change')
ylabel('Admittance (dB)')
xlabel('Frequency (MHz)')
%Plot Slab
plot(freqS,addmitanceS,'b')
plot(PeakSAFreq, PeakSAValue  ,'*k')
text(PeakSAFreq*1.01,PeakSAValue-1,'Slabs: QFac '+QFacTextSA+', Fc '+FreqStringSA+'
MHz')
plot(PeakSRFreq, PeakSRValue  ,'*k')
text(PeakSRFreq*1.01,PeakSRValue-1,'Slabs: QFac '+QFacTextSR+', Fc '+FreqStringSR+'
MHz')
%Plot No Slab
plot(freqN,addmitanceN,'r')
plot(PeakNAFreq, PeakNAValue  ,'*k')
text(PeakNAFreq*1.01,PeakNAValue+1,'No Slabs: QFac '+QFacTextNA+', Fc '+FreqStringNA+'
MHz')
plot(PeakNRFreq, PeakNRValue  ,'*k')
text(PeakNRFreq*1.01,PeakNRValue+1,'No Slabs: QFac '+QFacTextNR+', Fc '+FreqStringNR+'
MHz')
hold off
```

Appendix C

Material properties used for Aluminum Nitride and Lithium Niobate YX36°-cut,

Table 6.3 Material parameters used.

Parameter	*AlN (000-plane)*	*$LiNbO_3$ (YX36°-cut)*
Density $\left[\frac{kg}{m^3}\right]$	3300	4700
Relative Permittivity	$\begin{bmatrix} 9.208 & 0 & 0 \\ 0 & 9.208 & 0 \\ 0 & 0 & 10.119 \end{bmatrix}$	$\begin{bmatrix} 43.6 & 0 & 0 \\ 0 & 34.149 & 0 \\ 0 & 0 & 38.611 \end{bmatrix}$
Elasticity Matrix, Voigt Notation $[Pa]$	$\begin{bmatrix} 4.1 & 1.49 & 0.99 & 0 & 0 & 0 \\ 1.49 & 4.1 & 0.99 & 0 & 0 & 0 \\ 0.99 & 0.99 & 3{,}89 & 0 & 0 & 0 \\ 0 & 0 & 0 & 1.25 & 0 & 0 \\ 0 & 0 & 0 & 0 & 1.25 & 0 \\ 0 & 0 & 0 & 0 & 0 & 1.305 \end{bmatrix} * e11$	$\begin{bmatrix} 2.0289 & 0.5875 & 0.6907 & -0.1323 & 0 & 0 \\ 0.5875 & 2.2232 & 0.9033 & -0.0867 & 0 & 0 \\ 0.6907 & 0.9033 & 1.9279 & -0.0764 & 0 & 0 \\ -0.1323 & -0.0867 & -0.0764 & 0.7533 & 0 & 0 \\ 0 & 0 & 0 & 0 & 0.7824 & 0.0434 \\ 0 & 0 & 0 & 0 & 0.0434 & 0.5653 \end{bmatrix} * e11$
Coupling Matrix, Voigt Notation $\left[\frac{C}{m^2}\right]$	$\begin{bmatrix} 0 & 0 & 0 & 0 & -3.84 & 0 \\ 0 & 0 & 0 & -3.84 & 0 & 0 \\ -1.916 & -1.916 & 4.959 & 0 & 0 & 0 \end{bmatrix} * e-12$	$\begin{bmatrix} 0 & 0 & 0 & 0 & 0.1224 & -4.479 \\ -1.648 & -2.297 & 2.573 & 0.4670 & 0 & 0 \\ -1.939 & -1.591 & 4.527 & -0.2592 & 0 & 0 \end{bmatrix}$

Parameter	*Aluminium (000-plane)*	*Platinum (000-plane)*
Density $\left[\frac{kg}{m^3}\right]$	2700	21450
Relative Permittivity	1	1.000265
Young's Modulus $[Pa]$	70*e*9	168*e*9
Poisson's Ratio	0.35	0.38